100 exemplaires avec cette page de garde

(à envoyer directement au Centre de Recherche en Physique des Plasmas)

June 1976 LRP 105/76

NUMERICAL COMPUTATIONS OF THE MAGNETOHYDRODYNAMIC SPECTRUM FOR ONE AND TWO DIMENSIONAL EQUILIBRIA USING REGULAR FINITE ELEMENTS AND FINITE HYBRID ELEMENTS

R. Gruber

Centre de Recherches en Physique des Plasmas
ECOLE POLYTECHNIQUE FEDERALE DE LAUSANNE

June 1976 LRP 105/76

NUMERICAL COMPUTATIONS OF THE MAGNETOHYDRODYNAMIC SPECTRUM FOR ONE AND TWO DIMENSIONAL EQUILIBRIA USING REGULAR FINITE ELEMENTS AND FINITE HYBRID ELEMENTS

R. Gruber

ABSTRACT

Two new numerical schemes to calculate the ideal MHD spectrum of straight circular (1D) and non circular (2D) cross-section plasmas are described. They are based respectively on a regular finite element expansion and on a finite hybrid element expansion of the variational principle. In the low beta limit the low-frequency stable modes and all the unstable modes become nearly incompressible. Choosing different basis functions for the three components of the displacement vector (regular finite elements) such that exact incompressibility can be satisfied, allows an equally good representation of the stable and unstable part of the spectrum in the 1D case, for arbitrary values of beta. In the 2D case the regular finite element method is suitable to calculate the kink mode, but the slowly growing internal modes cannot be obtained at low beta with this method, because of a poor representation of the $\underline{B}\cdot\nabla$ operator. Another expansion scheme which uses different basis functions for the displacement and its derivatives (finite hybrid elements) is shown to remove all difficulties. Results of test cases are presented.

C O N T E N T S

I. INTRODUCTION

As a first step in assessing the value of a plasma confinement configuration, one must determine the stability behaviour in the ideal magnetohydrodynamic (MHD) [1] limit. Numerous stability criteria have been derived. For example, Newcomb [25] gave necessary and sufficient conditions for the stability of cylindrical plasmas. Suydam [2] derived a necessary criterion which tests the existance of unstable localized modes in a cylindrical plasma. Bineau [23] generalized the Newcomb criteria to toroidal configuration and Mercier [3] found a necessary criterion for axisymmetric configurations. In all these considerations the objective was to find stable configurations. The success of "unstable" configurations which show good confinement characteristics have led to a change of this point of view. The tokamaks, for example, can work with a safety factor q less than one on the axis. The internal kink is unstable in this case and gives rise to an anomalous heat transport [4], but it does not destroy the discharge. This is the reason why one is now interested in knowing more about a configuration than just a yes or no answer to its stability. One wants to know the growth rates of the instabilities and the corresponding eigenfunctions. The applicability of active stabilizing systems such as feedback is strongly conditioned by the shape of the eigenfunctions. Also one likes to know how the modes depend on the parameters of the machine. Only a numerical treatment of the full set of equations [24] can answer these questions. Recently many groups have started to develop general purpose codes to study the stability problem of straight and toroidal configurations.

The stability of a straight cylindrical plasma column of circular cross section in which the equilibrium quantities depend only on one variable (the radius) is fairly well understood. Codes have been written which compute, for a given equilibrium, growthrates of instabilities and corresponding eigenfunctions. These codes use either a shooting method [5,6], solving the Hain-Lüst equation [7] directly, or a finite element method [8,9]. The finite element method has the advantage that it gives quickly an overall view of the whole spectrum and thus permits a better qualitative understanding of

the dependence of the eigenfrequencies and the eigenmodes on the parameters of the configuration.

The main interest is now shifting to axisymmetric toroidal configurations of small aspect ratio with non-circular cross-sections. The equilibrium quantities for these plasmas are functions of two variables (radius and angle) so that the stability problem becomes two-dimensional. Stability criteria have been derived, such as the Mercier criterion [3]. The influence of toricity on the internal kink mode [10,11] and the effect of non-circularity [12] have been studied by expanding the potential energy in powers of the inverse aspect ratio or in powers of the ellipticity. A major disadvantage in all these analytic calculations is that growth rates and eigenmodes are obtained only qualitatively. The only possibility to obtain the actual growth rates and the eigenfunctions is to solve the MHD stability equations numerically. We distinguish between two main approaches the evolutionary method and the variational method.

The first successful codes to solve the ideal MHD stability equations were the time evolutionary codes [13,14,15]. In these calculations the linearized equations of motion are solved numerically by a finite difference scheme [16]. An initial equilibrium state is perturbed randomly and the asymptotic time behaviour of this initial noise is determined. This technique works well in the high-β regime and gives reasonable accuracy for the most unstable kink mode. The time evolutionary codes are inadequate for treating tokamak-like plasmas with a low-β . For such plasmas the growth rate of the most unstable mode is very small, and the coupling of this mode with the marginally stable modes of the continuum makes it impossible to extract the unstable mode in a reasonable time. One also finds that localized modes too can not be obtained with the time evolutionary codes. This is probably due to the choice of the coordinate system. A cartesian system does not fit the magnetic flux surfaces. As a consequence, a diffusion of the fluid elements through the flux surfaces takes place which results in a stabilizing mode coupling. The main advantage of the time evolutionary method is that the inclusion of dissipative effects is straight forward. It also constitutes

the first step towards obtaining a fully nonlinear code [17,18].

In the variational method the displacement vector is expanded in terms of a set of basis functions [19] and substituted into the Lagrangian of the system. Different choices of basis functions can lead to quite different methods. The Princeton group [26,27] has used global functions in the two dimensions and, in the last version of their code, a combination of a global Fourier expansion in the poloidal angle and a finite element expansion in the "radial" direction. The global expansion in the poloidal angle seems to be well suited to their nonorthogonal, so-called "natural", coordinate system [28] and to the straight elliptical problem that they solve.

The object of this work was to develop a general code which would use finite element expansions in both directions. The starting point was the paper by Takeda et al [8] in which the one-dimensional stability problem is solved numerically. All vector components were expanded in terms of linear finite elements. At first sight it appeared that this finite element approach was successful although they did mention difficulties in representing the eigenfunctions. Trying to reproduce their results we found that the eigenmodes are very poorly represented and that the growth rates become impossible to obtain in the low β limit with a reasonable number of intervals. In order to investigate these difficulties an analytically tractable test case was studied with this method [29]. It was found that the numerical spectrum did not converge towards the analytic spectrum. This so-called "spectrum pollution" [22] is responsible for the bad representation of the eigenfunctions and for the stabilization of the growing modes. Our first objective has been to develop a pollution free expansion scheme for the one-dimensional stability problem.

The solution was to choose different basis functions for the components of the displacement $\underset{\sim}{\xi}$ such that $\underset{\sim}{\nabla}\cdot\underset{\sim}{\xi} = 0$ can be satisfied everywhere [9]. This so-called "regular finite element" expansion removes all the pollution and permits an accurate description of the unstable modes. A

general purpose code has been written [20] and applied with success to a number of configurations.

We then applied the same receipe to the two-dimensional problem, choosing the "regular finite elements" in such a way that $\underline{\nabla} \cdot \underline{\xi} = 0$ can be satisfied everywhere. This expansion scheme has been tested with the same straight elliptical equilibrium as used by the Princeton group. For a small ellipticity the kink is well reproduced with a reasonable number of mesh cells [21]. However, the weakly growing internal modes are very difficult to obtain, even in the most favorable circular case. This new difficulty can be traced to a poor representation of the $\underline{B} \cdot \underline{\nabla}$ operator, which, in the one-dimensional case, was just a trivial number.

We then tried a completely different method for which we propose the name "finite hybrid elements". The basis idea is to consider the vector components and their derivatives as distinct variables which are only identified at specific points in each mesh cell. The basis functions are chosen in such a way that each term in the Lagragian has the same functional dependence. Until now this method has been only applied to a cylindrical geometry. No pollution has been observed. The weakly growing modes are obtained already with few points, even in situations where it was impossible to find them with the regular finite elements expansion. A quadratic convergence is observed already with few points in all the cases examined so far. We are confident that this method will work also in more complicated geometries.

In conclusion we have found that it is not possible to apply brutally the standard finite element method to the Lagrangian. The unstable modes are nearly incompressible and to correctly represent them it is necessary to respect this feature by an adequate approximation scheme. The finite hybrid element method proposed here as the ultimate solution may not be the only possibility, but it has shown computational advantages. It is well adapted to the study of numerically determined equilibria and it is easy to implement.

II. THE IDEAL MHD MODEL

1. The Basic Equations

In this model the plasma is treated as a perfectly conducting fluid, with no viscosity or thermal conductivity. The only body force is the Lorentz force. The set of equations reads

$$\frac{D\rho}{Dt} + \rho \nabla \cdot \underline{v} = 0 \qquad \text{(continuity)} \qquad (1)$$

$$\rho \frac{D\underline{v}}{Dt} = -\nabla p + \underline{J} \times \underline{B} \qquad \text{(Newton)} \qquad (2)$$

$$\frac{D}{Dt}\left(p \rho^{-\gamma}\right) = 0 \qquad \text{(adiabaticity)} \qquad (3)$$

$$\nabla \times \underline{B} = \underline{J} \qquad (4)$$

$$\nabla \times \underline{E} = -\frac{\partial \underline{B}}{\partial t} \qquad \text{(Maxwell)} \qquad (5)$$

$$\nabla \cdot \underline{B} = 0 \qquad (6)$$

$$\underline{E} + \underline{v} \times \underline{B} = 0 \qquad \text{(Ohm's Law)} \qquad (7)$$

ρ, p and $\underline{v}$ are respectively the density, pressure and velocity of the fluid and $\underline{J}$, $\underline{B}$ and $\underline{E}$ the current, the magnetic and electric fields. The natural system of units of Weibel [31] is used throughout this work. D/Dt denotes the convective derivative

$$\frac{D}{Dt} \equiv \frac{\partial}{\partial t} + \underline{v} \cdot \nabla . \qquad (8)$$

The displacement current has been neglected in Maxwell's equations in order to remain consistent with the low-frequency assumption which conditions the validity of the model. The pressure is assumed isotropic.

Equation (7) follows from the assumption of infinite conductivity and can be interpreted [32] as a freezing of the magnetic lines of force in the fluid.

2. Equilibrium

An equilibrium state is characterized by the conditions

$$\frac{\partial}{\partial t} = 0 \qquad ; \qquad \underline{v} = 0 \; . \tag{9}$$

We thus exclude stationary solutions with $\underline{v} \neq 0$ and $\partial \underline{v} / \partial t = 0$. Adding the index "0" to equilibrium quantities, we find that the remaining non-trivial MHD eqs. (1-7) become

$$\begin{aligned} \underline{\nabla} p_0 &= \underline{J}_0 \times \underline{B}_0 \\ \underline{\nabla} \times \underline{B}_0 &= \underline{J}_0 \\ \underline{E}_0 &= 0 \\ \underline{\nabla} \cdot \underline{B}_0 &= 0 \; . \end{aligned} \tag{10}$$

A confined plasma must have closed isobars, which do not intersect any material surface. Dotting the first equation in eq. (10) with $\underline{B}_0$ and $\underline{J}_0$, successively, shows that isobaric surfaces are also magnetic and current surfaces. Equations (10) have an infinite number of solutions, but there are no confinement configurations topologically equivalent to a sphere. The simplest possible configurations are toroidal. Note that mirror configurations are based upon anisotropic pressure effects and cannot be described by eqs. (10). We are interested in toroidal configurations and in straight infinite geometries. The latters are considered

as limits of a torus with an infinite radius. The plasma boundary has to be an isobar if there is vacuum around the plasma. Except where mentioned explicitely we shall always assume that the current density $\underline{J}_o$ is everywhere finite, which implies no surface currents, that $p_o = 0$ at the surface and that $\underline{B}_o$ is continuous across the boundary. As far as the plasma is concerned, the equilibrium only depends on $\underline{B}_o$ at the surface and not on $\underline{B}_o$ in the vacuum region.

3. Linearized Equations

Let us assume a plasma in equilibrium described by eqs. (10). If at time $t = 0$ the system is slightly displaced from this equilibrium it will, in general, evolve in time. As long as the displacement is small, we can study this evolution by linearizing the eqs. (1-7) around the equilibrium values. Defining by $\delta\varrho$, δp, $\underline{\delta B}$ and $\underline{\delta J}$, $\underline{E}$ and $\underline{v}$ the perturbations in the corresponding quantities, these equations become after elimination of $\delta\varrho$:

$$
\begin{aligned}
\varrho_o \frac{\partial \underline{v}}{\partial t} &= -\underline{\nabla}\delta p + \underline{\delta J} \times \underline{B}_o + \underline{J}_o \times \underline{\delta B} \\
\frac{\partial \delta p}{\partial t} &= -\underline{v} \cdot \underline{\nabla} p_o - \gamma p_o \underline{\nabla} \cdot \underline{v} \\
\underline{E} &= -\underline{v} \times \underline{B}_o \\
\underline{\nabla} \times \underline{\delta B} &= \underline{\delta J} \\
\underline{\nabla} \times \underline{E} &= -\frac{\partial}{\partial t} \underline{\delta B} \, .
\end{aligned}
\tag{11}
$$

Let us introduce the Lagrangian displacement $\underline{\xi}(\underline{r}_o, t)$

$$
\underline{r}(t) = \underline{r}_o + \underline{\xi}(\underline{r}_o, t)
$$

and

$$\underline{v}(\underline{r}, t) = \frac{\partial \underline{\xi}}{\partial t}(\underline{r}_o, t), \tag{12}$$

where $\underline{r}_o$ is the unperturbed location of the fluid element which is at $\underline{r}$ at time t. The vectors $\underline{r}_o$ and $\underline{r}$ only differ by $\underline{\xi}$ so that we can replace $\underline{r}$ by $\underline{r}_o$ in the coefficients of eqs. (11). These equations become after a partial time integration:

$$\begin{aligned}
\rho_o \frac{\partial^2 \underline{\xi}(\underline{r}, t)}{\partial t^2} &= -\underline{\nabla}\delta p + \underline{\delta J} \times \underline{B}_o + \underline{J}_o \times \underline{\delta B} \\
\delta p &= -\underline{\xi} \cdot \underline{\nabla} p_o - \gamma p_o \underline{\nabla} \cdot \underline{\xi} \\
\underline{\delta J} &= \underline{\nabla} \times \underline{\delta B} \\
\underline{\delta B} &= \underline{\nabla} \times (\underline{\xi} \times \underline{B}_o) .
\end{aligned} \tag{13}$$

By substituting the last three equations into the first equation in (13), we obtain the equation of evolution for $\underline{\xi}(\underline{r}, t)$

$$\rho_o \frac{\partial^2 \underline{\xi}}{\partial t^2} = \underline{F}[\underline{\xi}], \tag{14}$$

where

$$\begin{aligned}
\underline{F}[\underline{\xi}] \equiv\ & \underline{\nabla}(\gamma p_o \underline{\nabla} \cdot \underline{\xi} + \underline{\xi} \cdot \underline{\nabla} p_o) + \\
& + \underline{J}_o \times [\underline{\nabla} \times (\underline{\xi} \times \underline{B}_o)] + \{\underline{\nabla} \times [\underline{\nabla} \times (\underline{\xi} \times \underline{B}_o)]\} \times \underline{B}_o .
\end{aligned} \tag{15}$$

$\underline{F}$ is a linear time independent operator. In the vacuum region the perturbed magnetic field $\underline{\delta B}_v$ satisfies Maxwell's equations

$$\underline{\nabla} \cdot \underline{\delta B_v} = 0$$
$$\underline{\nabla} \times \underline{\delta B_v} = 0 \quad , \tag{16}$$

with the condition that $\underline{\delta B_n}$ be continuous across the plasma surface

$$\underline{\hat{n}} \cdot \underline{\delta B_v} = \underline{\nabla} \times \left(\xi_n \, \underline{\hat{n}} \times \underline{B_o} \right) . \quad \text{(plasma)} \tag{17}$$

A second boundary condition for $\underline{\delta B_v}$ is obtained by assuming the system is surrounded by a perfectly conducting shell on which

$$\underline{\delta B_v} \cdot \underline{\hat{n}} = 0 . \quad \text{(shell)} \tag{18}$$

It is this shell which isolates the whole system and makes it conservative. Equations (16), (17) and (18) determine $\underline{\delta B_v}$ as a linear functional of ξ_n on the plasma surface. There is a last boundary condition which has to be applied on the plasma surface, i.e. the continuity of the total pressure $p + |B|^2/2$. It is

$$-\underline{\xi} \cdot \underline{\nabla} p_o + \gamma p_o \, \underline{\nabla \cdot \xi} + \underline{B_o} \cdot \underline{\delta B} = \underline{B_o} \cdot \underline{\delta B_v} . \tag{19}$$

Substitution of $\underline{\delta B}$ and $\underline{\delta B_v}$ in terms of $\underline{\xi}$ into equation (19) gives a homogeneous, but non-local, condition on $\underline{\xi}$ at the surface. This is the boundary condition which has to be added to eq. (14) to make the problem well defined. Equations (14) and (19) admit solutions of the form

$$\underline{\xi}(\underline{r}, t) = \underline{\xi}(\underline{r}) \, e^{i\omega t} , \tag{20}$$

where $\underline{\xi}(\underline{r})$ can be chosen real. The equation of motion (14)

$$-\omega^2 \rho_o \, \underline{\xi}(\underline{r}) = \underline{F}\left[\underline{\xi}(\underline{r})\right] , \tag{21}$$

together with the boundary condition (19), constitutes an eigenvalue problem. $\underline{F}$ is a symmetric linear operator [32], which implies that ω^2 be real. The unstable part of the spectrum corresponds to $\omega^2 < 0$.

4. Variational Formulation

Excluding the modes of deformation which change the total current flowing in the plasma by imposing the constraint

$$\oint \underline{\delta B_v} \cdot \underline{d\ell} = 0 \quad , \tag{22}$$

equations (16-18) may be rewritten as

$$\begin{aligned} \underline{\delta B_v} &= \underline{\nabla} \phi \\ \underline{\nabla}^2 \phi &= 0 \quad , \end{aligned} \tag{23}$$

with the boundary conditions

$$\begin{aligned} \frac{d\phi}{dn} &= 0 \qquad \text{(shell)} \\ \frac{d\phi}{dn} &= \left[\underline{\nabla} \times \left(\xi_n \hat{\underline{n}} \times \underline{B_e} \right) \right]_n \quad . \qquad \text{(plasma)} \end{aligned} \tag{24}$$

Here, ξ_n is the normal component of the displacement and ϕ is a continuous function of $\underline{r}$. A solution of eqs. (23) can be written in terms of a Green function $G(\underline{r}/\underline{r}_s)$, where the index s refers to a point on the plasma surface, by

$$\phi(\underline{r}) = \int_S \underline{d\sigma_s} \cdot \underline{\nabla} \phi(\underline{r_s}) \, G(\underline{r}/\underline{r_s}) \quad , \tag{25}$$

where $G(\underline{r}/\underline{r}_s)$ is real and symmetric.

The eigenvalue problem (19, 21) can be reformulated as a variational problem [24,25]

$$\delta L = \delta \left[W_p + W_v - W_k \right] = 0 \ , \tag{26}$$

where

$$W_p = \int_{\text{plasma}} \frac{1}{2} d^3r \left\{ \left[\nabla \times (\underline{\xi} \times \underline{B}_o) + (\underline{\xi} \cdot \hat{\underline{n}}) (\underline{J}_o \times \hat{\underline{n}}) \right]^2 - \right.$$
$$\left. - 2 (\underline{\xi} \cdot \hat{\underline{n}})^2 (\underline{J}_o \times \hat{\underline{n}}) \cdot (\underline{B}_o \cdot \nabla) \hat{\underline{n}} + \gamma p_o (\nabla \cdot \underline{\xi})^2 \right\} \tag{27}$$

$$W_v = \iint \frac{1}{2} G(\underline{r}_s/\underline{r}_s') \left[d\underline{\sigma}_s \cdot \nabla \times (\xi_n \hat{\underline{n}} \times \underline{B}_o) \right] \cdot$$
$$\cdot \left[d\underline{\sigma}_s' \cdot \nabla' \times (\xi_n' \hat{\underline{n}}' \times \underline{B}_o') \right] \tag{28}$$

$$W_k = \int \frac{\omega^2}{2} d^3r \, \rho_o(\underline{r}) \, |\underline{\xi}|^2 \tag{29}$$

and $\hat{\underline{n}}(\underline{r})$ is an unit vector in the direction of ∇p_o, normal to the equilibrium magnetic surface which contains $\underline{r}$. The energies W_p, W_v and W_k are quadratic forms in $\underline{\xi}$. In W_p the components of $\underline{\xi}$ tangential to the magnetic surface appear with only tangential derivatives. This means that these components may be discontinuous across a magnetic surface. Therefore in the variation given in eq. (24), ξ_n must be continuous and differentiable in any direction, while the other two components of $\underline{\xi}$ must be continuous and differentiable only along the magnetic surface. Discontinuities along ∇p_o are allowed.

As the conducting shell approaches the plasma surface the Green function becomes larger. In the limit of a perfectly tight conducting shell around the plasma it becomes infinite, thus forcing ξ_n to vanish identically on the plasma surface. In this case, which we call the "wall constrained" case, we impose $\xi_n = 0$ at the surface, as an additional condition on $\underset{\sim}{\xi}$, and drop W_v in eq. (26).

5. Axisymmetric Equilibrium

We are interested in axisymmetric equilibria with a single magnetic axis.

Toroidal geometry described by cylindrical coordinates (r, z, θ)

Cut of the same configuration by a meridian plane showing the non cartesian ψ, χ coordinate system. R is the radius of the magnetic axis and R/a is the aspect ratio.

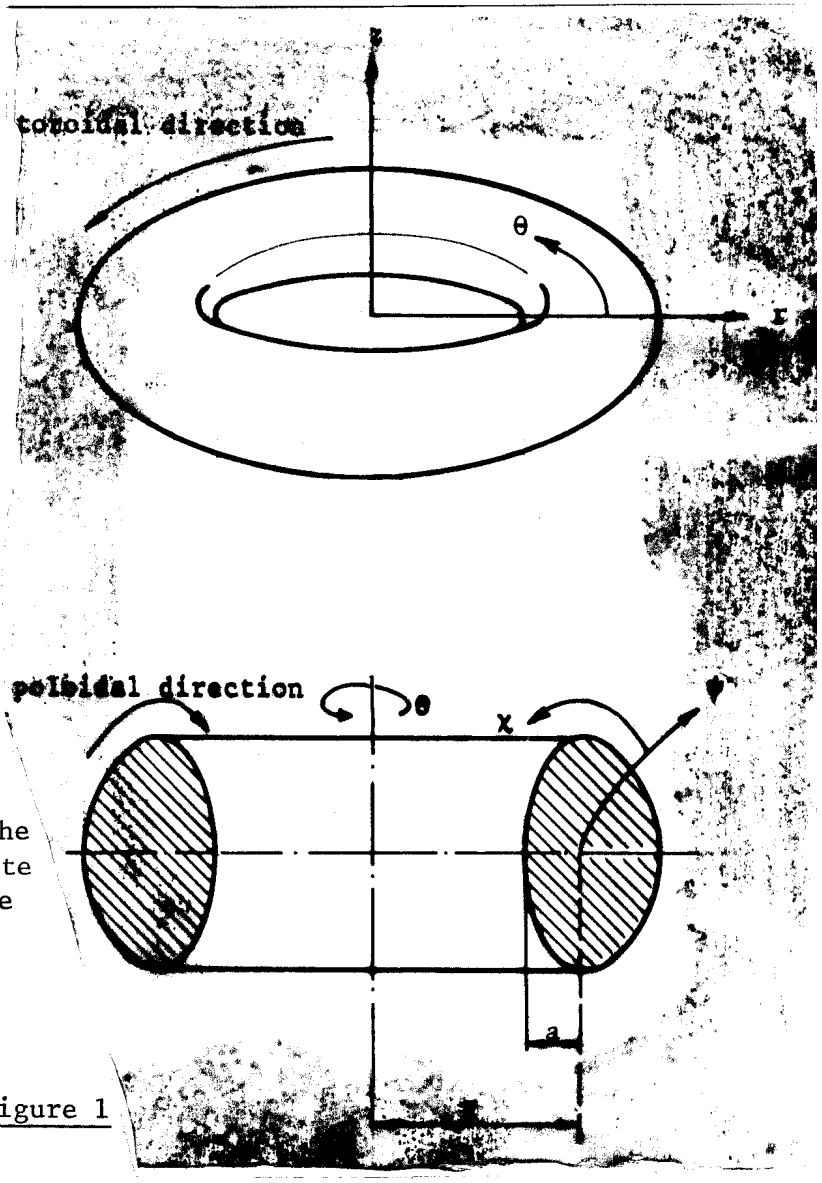

Figure 1

Using cylindrical coordinates (r,θ,z) in which the z axis coïncides with the axis of symmetry all possible equilibria can be described by [3]

$$\underline{B}_o = \frac{T(\psi)}{r}\,\hat{\underline{e}}_\theta + \frac{1}{r}\,\underline{\nabla}\psi(r,z) \times \hat{\underline{e}}_\theta$$
$$p_o = p_o(\psi) \quad , \tag{30}$$

where the function $\psi(r,z)$ is expressed in terms of the two arbitrary functions $p_o(\psi)$ and $T(\psi)$ by the pressure balance equation (10)

$$\frac{\partial^2\psi}{\partial z^2} + r\frac{\partial}{\partial r}\left(\frac{1}{r}\frac{\partial\psi}{\partial r}\right) = -\left(r^2 p' + TT'\right) \quad . \tag{31}$$

Here, the prime denotes a derivative with respect to ψ. We also assume that $\rho_o(\psi)$ depends only on ψ.

The r,z,θ coordinate system is replaced by a non cartesian orthogonal coordinate system ψ, χ, θ [33] as shown in Fig. 1. The knowledge of $\psi(r,z)$ determines completely the mesh but there remains an indeterminacy in the labeling of the surfaces χ = constant. The χ direction is always referred to as the poloidal direction. The volume element is written

$$d\tau = r\,dr\,d\theta\,dz = J\,d\psi\,d\theta\,d\chi \quad , \tag{32}$$

which defines the Jacobian $J(\psi,\chi)$. All equilibrium quantities are now assumed to be expressed in terms of ψ and χ. In these coordinates the operator grad becomes

$$\underline{\nabla} = r\,B\,\hat{\underline{e}}_\psi\frac{\partial}{\partial\psi} + \frac{1}{r}\,\hat{\underline{e}}_\theta\frac{\partial}{\partial\theta} + \frac{1}{JB}\,\hat{\underline{e}}_\chi\frac{\partial}{\partial\chi} \quad , \tag{33}$$

where

$$B = \frac{1}{r}\,\underline{\nabla}\psi \times \hat{\underline{e}}_\theta \tag{34}$$

is the poloidal field.

The current density $\underline{J}_o$ can then be expressed as

$$\underline{J}_o = \underline{\nabla} \times \underline{B}_o = j\,\underline{\hat{e}}_\theta + B T' \underline{\hat{e}}_x \,, \tag{35}$$

where

$$j = p'r + \frac{TT'}{r} = -\frac{r}{J}\frac{\partial}{\partial \psi}(JB^2). \tag{36}$$

We introduce a new displacement vector $\hat{\underline{\xi}}$ such that

$$\hat{\underline{\xi}} = \begin{pmatrix} X \\ Y \\ Z \end{pmatrix} = \begin{pmatrix} r B J \xi_\psi \\ J \xi_\theta / r \\ \xi_x / B \end{pmatrix} . \tag{37}$$

Since the equilibrium quantities do not depend on θ, solutions of equation (26) have the form

$$\hat{\underline{\xi}}^n(\underline{r}) = Re\left[\hat{\underline{\xi}}^n(\psi, x)\, e^{in\theta}\right] . \tag{38}$$

Replacing $\underline{\xi}$ in the variation principle (26) by the expression (38), the potential energies W_p and W_v become

$$\begin{aligned} W_p = \frac{\pi}{2} \iint d\psi\, dx \Big\{ & \frac{1}{J r^2 B^2} \left| \frac{\partial \frac{X}{J}}{\partial x} + \frac{in T}{r^2} X \right|^2 + \\ & + \frac{r^2}{J} \left| \frac{\partial \frac{Y}{J}}{\partial x} - \frac{\partial \frac{zT}{r^2}}{\partial x} - T \frac{\partial \frac{X}{r^2}}{\partial \psi} \right|^2 + \\ & + JB^2 \left| \frac{in Y}{J} - \frac{in T z}{r^2} + \frac{\partial \frac{X}{J}}{\partial \psi} + \frac{jX}{rJB^2} \right|^2 + \\ & + \gamma p_o \left| \frac{\partial X}{\partial \psi} + in Y + \frac{\partial z}{\partial x} \right|^2 - 2\frac{K}{J}|X|^2 \Big\} \end{aligned} \tag{39}$$

with

$$K = \frac{TT'}{r^2}\frac{\partial \log r}{\partial \psi} - \frac{j}{r}\frac{\partial \log(BJ)}{\partial \psi} \quad , \tag{40}$$

and

$$W_v = \frac{\pi}{2}\iint G_s(\chi/\chi')\left(\frac{\partial \frac{\chi}{J}}{\partial \chi} - \frac{inT}{r^2}\chi\right)_{\chi}\left(\frac{\partial \frac{\chi^*}{J}}{\partial \chi} + \frac{inT}{r^2}\chi^*\right)_{\chi'} d\chi d\chi' . \tag{41}$$

The kinetic energy W_k is written

$$W_K = \omega^2\frac{\pi}{2}\iint J\rho_0(\psi)\left\{\left|\frac{\chi}{rBJ}\right|^2 + \left|\frac{rY}{J}\right|^2 + |ZB|^2\right\} d\psi d\chi . \tag{42}$$

For simplicity the index n on X, Y and Z has been omitted.

The choice of the coordinate system together with the variable transformation (37) implies the regularity conditions

$$\chi(0,\chi) = 0 . \tag{43}$$

For a wall constrained plasma $W_v = 0$ and we have to impose the condition

$$\chi(\psi_s, 0) = 0 . \tag{44}$$

III. RITZ-GALERKIN APPROACH

Equations (39-44) are solved by expanding the displacement vector $\hat{\underline{\xi}}(\Psi,\chi) = (X,Y,Z)^T$ in terms of sufficient regular basis functions. The vector components are represented by

$$\begin{aligned} X &= \sum_{\ell} X_\ell \, e_\ell^x(\Psi,\chi) \\ Y &= \sum_{\ell} Y_\ell \, f_\ell^y(\Psi,\chi) \\ Z &= \sum_{\ell} Z_\ell \, f_\ell^z(\Psi,\chi) . \end{aligned} \tag{45}$$

When treating the variational problem with finite hybrid elements, we have to formulate an approach for describing each of the displacement components and an alternate description for their derivatives.

The Green function $G(\underline{r}/\underline{r}_s)$ in the vacuum contribution W_v in equation (41) is defined by equation (25). $G(\underline{r}/\underline{r}_s)$ can either be obtained analytically as in the one-dimensional case, or has to be calculated numerically. We decide from case to case how $G(\underline{r},\underline{r}_s)$ is to be obtained. In our 2D calculations it is also computed by a finite element expansion.

IV. THE CYLINDRICAL GEOMETRY

1. Reduction to a 1D Problem

In the limit of an infinite aspect ratio a circular cross-section torus becomes a straight circular plasma column. Instead of the ψ, χ, θ coordinate system we use the conventional cylindric coordinates shown in Fig. 2. The correspondance between the toroidal quantities and the cylindrical notation is given in Table I.

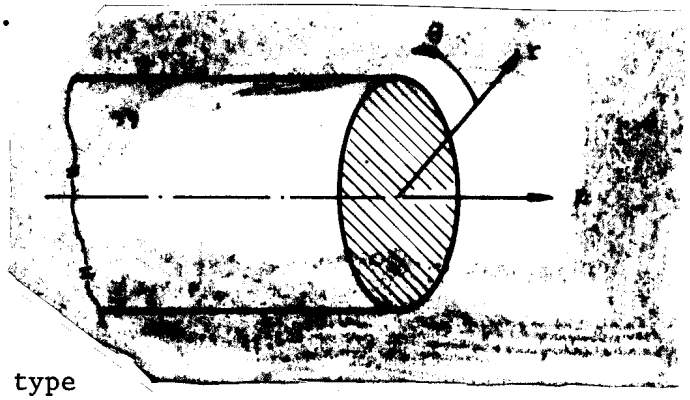

Figure 2: Cylindrical coordinates (r, θ, z) in a straight infinitely long ($a_r \to \infty$) geometry.

We perform a normal mode analysis of the type

$$\underline{\xi}(\underline{r}, t) = \underline{\xi}(r)\, e^{i\omega t + im\theta + ikz}, \tag{46}$$

where

$$\underline{\xi}(r) = (\xi_r, \xi_\theta, \xi_z)^T .$$

The general axisymmetric variational form, eqs. (39-44), can be transformed into the expressions given by Bernstein [24] or Newcomb [25]:

$$W_p = \int_0^{r_s} r\,dr \left\{ \Lambda(\xi_r, \xi_r') + \gamma^2 p_0 \left[\eta + \frac{1}{r}(r\xi_r)'\right]^2 + \right. \tag{47}$$
$$\left. + \frac{k^2 r^2 + m^2}{r^2} \left[J - J_0(\xi_r, \xi_r') \right]^2 \right\}$$

TABLE I: Correspondance between the toroidal and cylindrical coordinates

Toroidal Geometry		Cylindrical Geometry
$\frac{d\Psi}{rB}$	⟶	dr
χ	⟶	θ
$r\theta$	⟶	z
B	⟶	B_θ
$\frac{T}{r}$	⟶	B_z
$\frac{n}{r}$	⟶	k
JB	⟶	r

$$W_V = \frac{r_s Z(r_s)}{Z'(r_s)} F^2(r_s) \xi_r^2(r_s) \tag{48}$$

$$W_K = \int_0^{r_s} \omega^2 \rho_0 |\xi|^2 r\, dr \quad . \tag{49}$$

The prime denotes $\frac{d}{dr}$ and Λ, ξ_0, η, ξ and F are defined as follows:

$$\mathcal{L}\left(\xi_r\,,\,\xi_r'\right) = \frac{1}{k^2r^2+m^2}\left[\,Fr\,\xi_r' + \left(k\,B_z - \frac{m}{r}\,B_\theta\right)\xi_r\right]^2 +$$

$$+\;F^2\xi_r^2 \;-\; 2\,B_\theta\,(r\,B_\theta)'\,\frac{\xi_r^2}{r^2} \qquad (50)$$

$$\mathcal{J}_o\left(\xi_r\,,\,\xi_r'\right) = \frac{r}{k^2r^2+m^2}\left[\left(k\,B_\theta - \frac{m}{r}B_z\right)r\xi_r' - \left(k\,B_\theta + \frac{m}{r}\,B_z\right)\xi_r\right],$$

$$\eta \;=\; \frac{im}{r}\,\xi_\theta \;+\; i\,k\,\xi_z$$

$$\mathcal{J} \;=\; i\,\xi_\theta\,B_z \;-\; i\,\xi_z\,B_\theta \qquad (51)$$

$$F \;=\; k\,B_z \;+\; \frac{m}{r}\,B_\theta\;.$$

The function Z(r), in the expression for the vacuum energy (48), is a solution of Bessel's equation of order 0 such that $Z'(r_w) = 0$, where r_w is the radius of the conducting shell. Note that ξ_r , η and $\mathcal{J}$ can be chosen real without loss of generality [25]. This implies that ξ_θ and ξ_z are pure imaginary.

An alternate form of the potential energy W_p is [3]

$$W_p \;=\; \int_0^{r_s} r\,dr\left\{\,F^2\xi_r^2 + \left[\,B_z\,D - iF\xi_z\right]^2 + \left[\,B_\theta\,D - iF\xi_z - 2\,\frac{B_\theta}{r}\,\xi_r\right]^2 + \right.$$

$$\left. +\;\gamma p_o\,D^2 \;-\; 2\,B_\theta\,(r\,B_\theta)'\,\frac{\xi_r^2}{r^2}\,\right\}, \qquad (52)$$

where

$$D = \underline{\nabla} \cdot \underline{\xi} = \frac{1}{r}(r\xi_r)' + \frac{im}{r}\xi_\theta + ik\xi_z \ . \tag{53}$$

The representation given by equations (47-49) is very useful for an analytic treatment of the marginal case $\omega^2 = 0$. In this case the variations in ξ_r, η and ζ decouple yielding two algebraic equations for η and ζ

$$\begin{aligned} \underline{\nabla} \cdot \underline{\xi} &= \eta + \frac{1}{r}(r\xi_r)' = 0 \\ \zeta - \zeta_0(\xi_r, \xi_r') &= 0 \ , \end{aligned} \tag{54}$$

and a variational form for ξ_r:

$$\delta \int_0^{r_s} \Lambda(\xi_r, \xi_r')\, r\, dr + \delta W_v = 0 \ . \tag{55}$$

These equations were the starting point of much analytic work on MHD stability in the last two or three decades. The idea has been to construct unstable test functions from exact solutions of (55). Suydam, for example, applied this method to find his stability criterion [2]. In order to better understand the difficulties encountered in the numerical determination of the spectrum, we first look at the general structure of the spectrum by analytical means. We then compute in detail a simple test case which will serve as a reference test for comparing the various approximation schemes.

2. General Spectral Properties

Equations (13) describe the MHD behavior while the equilibrium quantities are obtained from the pressure balance eqs. (10). Replacing $\underline{\xi}(\underline{r})$ by its expression (46) and eliminating $\underline{E}$ and $\underline{J}$ in the eqs. (10) reduce to a system of seven equations for the seven variable ξ_r, ξ_θ, ξ_z, δp, δB_r, δB_θ and δB_z. Introducing the new variable

$$P = \delta p + \underline{B_o} \cdot \underline{\delta B} = \delta p + B_\theta \delta B_\theta + B_z \delta B_z \tag{56}$$

the set of equations can be written as

$$-\omega^2 \rho_o \xi_r + P' - iF \delta B_r + \frac{2}{r} B_\theta \delta B_\theta = 0$$

$$-\omega^2 \rho_o \xi_\theta + \frac{im}{r} P - \frac{1}{r}(r B_\theta)' \delta B_r - iF \delta B_\theta = 0$$

$$-\omega^2 \rho_o \xi_z + ikP - B_z' \delta B_r - iF \delta B_z = 0$$

$$\delta p + p_o' \xi_r + \gamma p_o \left[\frac{1}{r}(r\xi_r)' + \frac{im}{r}\xi_\theta + ik\xi_z \right] = 0 \tag{57}$$

$$\delta B_r - iF\xi_r = 0$$

$$\delta B_\theta + (B_\theta \xi_r)' - ikB_z \xi_\theta + ikB_\theta \xi_z = 0$$

$$\delta B_z + \frac{1}{r}(r B_z \xi_r)' + \frac{im}{r} B_z \xi_\theta - \frac{im}{r} B_\theta \xi_z = 0 \ .$$

After elimination of five purely algebraic equations, we obtain two coupled ordinary first order differential equations [34].

$$N\,(r\xi_r)' = C_1\, r\xi_r - r\,C_2\,P$$
$$N\,P' = \frac{1}{r}\,C_3\, r\xi_r - C_1\,P\,. \tag{58}$$

Here

$$N = (\rho_0\omega^2 - F^2)\left[\rho_0\omega^2\left(\gamma p_0 + B_0^2\right) - \gamma p_0 F^2\right]$$
$$C_1 = \frac{2B_\theta}{r}\left\{\rho_0^2\omega^4 B_\theta - \frac{m}{r}F\left[\rho_0\omega^2\left(\gamma p_0 + B_0^2\right) - \gamma p_0 F^2\right]\right\}$$
$$C_2 = \rho_0^2\omega^4 - \left(k^2 + \frac{m^2}{r^2}\right)\left[\rho_0\omega^2\left(\gamma p_0 + B_0^2\right) - \gamma p_0 F^2\right] \tag{59}$$
$$C_3 = N\left[\rho_0\omega^2 - F^2 + 2B_\theta\left(\frac{B_\theta}{r}\right)'\right] +$$
$$+ \rho_0\omega^2\left(\rho_0\omega^2 - F^2\right)\left(\frac{2B_\theta}{r}\right)^2 - \left[\gamma p_0\left(\rho_0\omega^2 - F^2\right) + \rho_0\omega^2 B_z^2\right]\left(\frac{2B_\theta F}{r}\right)^2$$

and $B_0^2 = B_\theta^2 + B_z^2$. Equations (58) are equivalent to the second order differential equation of Hain and Lüst [7] and Goedbloed and Hagebeuk [35]:

$$\frac{d}{dr}\left[\frac{N}{C_2 r}\frac{d}{dr}(r\xi_r)\right] + \left[\frac{1}{N}\left(C_3 - \frac{C_1^2}{C_2}\right) - r\frac{d}{dr}\left(\frac{C_1}{rC_2}\right)\right]\xi_r = 0. \tag{60}$$

Equation (60) has been obtained by eliminating P from equations (58). We also can eliminate ξ_r and obtain another second order differential equation for P:

$$\frac{d}{dr}\left(\frac{rN}{C_3}\frac{dP}{dr}\right) - \left[\frac{r}{N}\left(C_2 - \frac{C_1^2}{C_3}\right) - \frac{d}{dr}\left(\frac{rC_1}{C_3}\right)\right]P = 0. \quad (61)$$

Defining ω_A^2 and ω_s^2 by

$$N \equiv \rho_0^2\left(\gamma p_0 + B_0^2\right)\left(\omega^2 - \omega_A^2\right)\left(\omega^2 - \omega_s^2\right), \quad (62)$$

one sees from eqs. (58-61) that N = 0 gives rise to two continua: The Alfvèn wave continuum

$$0 \leq \min_{0\leq r\leq r_s}\left(F^2/\rho_0\right) \leq \omega_A^2 \leq \max_{0\leq r\leq r_s}\left(F^2/\rho_0\right), \quad (63)$$

and the slow wave continuum

$$0 \leq \min_{0\leq r\leq r_s}\left[\gamma p_0 F^2/(\gamma p_0 + B_0^2)\right] \leq \omega_s^2 \leq \max_{0\leq r\leq r_s}\left[\gamma p_0 F^2/(\gamma p_0 + B_0^2)\right]. \quad (64)$$

Note that the continua are always stable ($\omega^2 \geq 0$).

At first glance, $C_2 = 0$ in equation (60) and $C_3 = 0$ in equation (61) could also yield continua. Equation (58) show that this is not the case [34]. If $C_2 = 0$, or $C_3 = 0$, one equation in (58) is simply decoupled from the other equation. Goedbloed [36] studied the significance of $C_2 = 0$. Calling ω_3^2 and ω_4^2 the two roots of $C_2 = 0$, he showed that $\omega^2 = \omega_3^2$ and $\omega^2 = \omega_4^2$ are the "separators" of the slow wave continuum from the Alfvèn continuum, and of the Alfvèn continuum from the dense point (accumulation point or infinitely degenerate spectral point) [37] of the fast wave spectrum ($\omega_F^2 = \infty$), respectively. A similar discussion can be given for $C_3 = 0$.

But here we obtain three "separators": ω_5^2, ω_6^2 and ω_7^2. Again one finds that $\omega^2 = \omega_6^2$ separates the slow wave continuum from the Alfvèn continu-

um (similar to $\omega^2 = \omega_3^2$) and that $\omega^2 = \omega_7^2$ has a similar meaning to $\omega^2 = \omega_4^2$ (see Fig. 3). The third "separator" $\omega^2 = \omega_5^2$ is below the slow wave continuum.

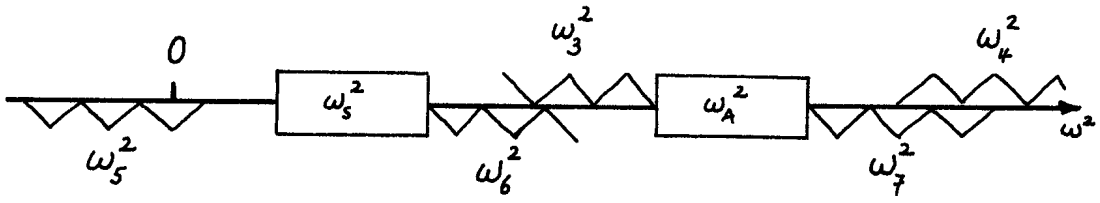

Figure 3: Schematic representation of the different continua and the "separator regions" of the 1D MHD spectrum. The discrete modes, which depend on the choice of the boundary conditions, can be everywhere.

There is also a discrete part of the spectrum. It depends on the boundary conditions. The only general statement which can be made is that the eigenfrequencies have a lower bound.

3. The Test Case

The most simple straight circular equilibrium is a wall constrained plasma without any current flowing along the cylinder axis. We assume constant density and constant longitudinal magnetic field: $B_\theta = 0$, $B_z =$ constant, $\underline{J}_o = 0$, $\rho_o =$ constant. The spectrum of this simple case can be calculated analytically [29].

We choose $B_z = \rho_o = r_s = 1$ which implies that ω^2 is normalized by the Alfvèn transit frequency $\omega_a^2 = \frac{B_z^2}{\rho_o r_s^2}$. Normalizing the radius r to r_s, the pressure p_o to B_z^2 and the longitudinal wave number k to r_s^{-1}, eq. (60) becomes

$$(\omega^2 - k^2)\left\{\frac{d}{dr}\left[\frac{\omega^2(\gamma p_0 + 1) - \gamma p_0 k^2}{C_2 r}\ \frac{d}{dr}(r\xi_r)\right] + \xi_r\right\} = 0. \qquad (65)$$

The infinitely degenerate solution

$$\begin{aligned} \omega^2 &= k^2 \\ \xi_z &= \delta B_z = P = \underline{\nabla}\cdot\underline{\xi} = 0 \\ \delta B_r &= ik\xi_r \\ \delta B_\theta &= ik\xi_\theta \end{aligned} \qquad (66)$$

is called the Alfvèn class.

The incompressibility condition

$$\underline{\nabla}\cdot\underline{\xi} = 0 \qquad (67)$$

relates ξ_r to ξ_θ. It is possible to choose one component of the displacement and calculate the other using equation (67).

The two other classes of the spectrum have $\omega^2 \neq k^2$, $\xi_z \neq 0$ and $\underline{\nabla}\cdot\underline{\xi} \neq 0$. We then have to solve the second order differential equation

$$\frac{d}{dr}\left[\frac{\omega^2(\gamma p_0 + 1) - \gamma p_0 k^2}{C_2 r}\ \frac{d}{dr}(r\xi_r)\right] + \xi_r = 0 \qquad (68)$$

restricted by $\xi_r(1) = 0$ and $r\,\xi_r(0) = 0$.

The solution is

$$\xi_r(r) = c \cdot J_m'(Kr)$$

$$K^2 = \frac{(\omega^2 - k^2)(\omega^2 - \gamma p_0 k^2)}{\omega^2(1+\gamma p_0) - \gamma p_0 k^2} \quad . \tag{69}$$

The boundary condition $J_m'(K) = 0$ leads to the dispersion relation

$$\omega_{F,S}^2 = \frac{1}{2}(k^2 + \gamma_{m,\alpha}^2)(1+\gamma p_0)\left[1 \pm \sqrt{1 - \frac{4\gamma p_0}{(1+\gamma p_0)^2}\frac{k^2}{k^2+\gamma_{m,\alpha}^2}}\right]. \tag{70}$$

Here $\gamma_{m,\alpha}$ is the α^{th} zero of the radial derivative of the Bessel function of order m. The plus sign in (70) describes the fast-wave class (F) and the minus sign the slow-waves (S). One finds that ω_F^2 grows monotonically with α, i.e. with the number of zeros of the radial eigenfunctions; whereas, ω_s^2 falls monotonically towards the accumulation point $\gamma p_o\, k^2/(1 + \gamma p_o)$.

4. Linear Finite Elements

Takeda et al [8] proposed the method of finite elements to calculate the MHD instabilities. They were able to compute with a reasonable accuracy the growthrates of the fastest growing modes (kink) which arise in a Tokamak-like configuration with a conducting shell sufficiently far from the plasma surface. They met problems near the plasma surface which they solved by accumulating mesh points in this region. They also compared with the analytic results obtained by Shafranov [38] in the limit of an incompressible flow for a wall

constrained plasma. The agreement is poor and, as we have shown [29], the eigenfunctions are very badly represented. This paper was the starting point of this work. The first objective is to understand these problems by considering the analytically tractable case, discussed in section 2. This case contains the infinitely degenerate Alfvèn class characterized by an incompressible displacement vector ($\underline{\nabla} \cdot \underline{\xi} = 0$). Incompressibility is also a feature of a marginal displacement where $\omega^2 = 0$ (see eq. 54). Weakly unstable modes have nearly divergence-free displacement vectors and, therefore, are part of the Alfvèn class. We believe that it is crucial to describe the Alfvèn class as accurate as possible in order to obtain a reasonable description of the growing modes.

In our previous work [29] we discretize the variational principle (26), with the expressions (47-51) for the energies, in the same way as Takeda et al. The same linear basis functions $e_j(r)$ are chosen for all three vector components

$$\underline{\xi}(r) = \sum_{j=0}^{n} \begin{pmatrix} \xi_r^j \\ i\,\xi_\theta^j \\ i\,\xi_z^j \end{pmatrix} e_j(r) \,, \tag{71}$$

with

$$e_j(r) \quad 0 \le j \le n = \left\{ \begin{array}{ll} 0 & , \quad r < 0 \quad or \quad r < r_{j-1} \\ \dfrac{r - r_{j-1}}{r_j - r_{j-1}} & , \quad r_{j-1} \le r \le r_j \\ \dfrac{r - r_{j+1}}{r_j - r_{j+1}} & , \quad r_j \le r \le r_{j+1} \\ 0 & , \quad r > 1 \quad or \quad r > r_{j+1} \end{array} \right\} , \tag{72}$$

in which we have labeled the mesh points such that $0 = r_o < r_1 \ldots < r_n = 1$. The elements are shown in Fig. 4.

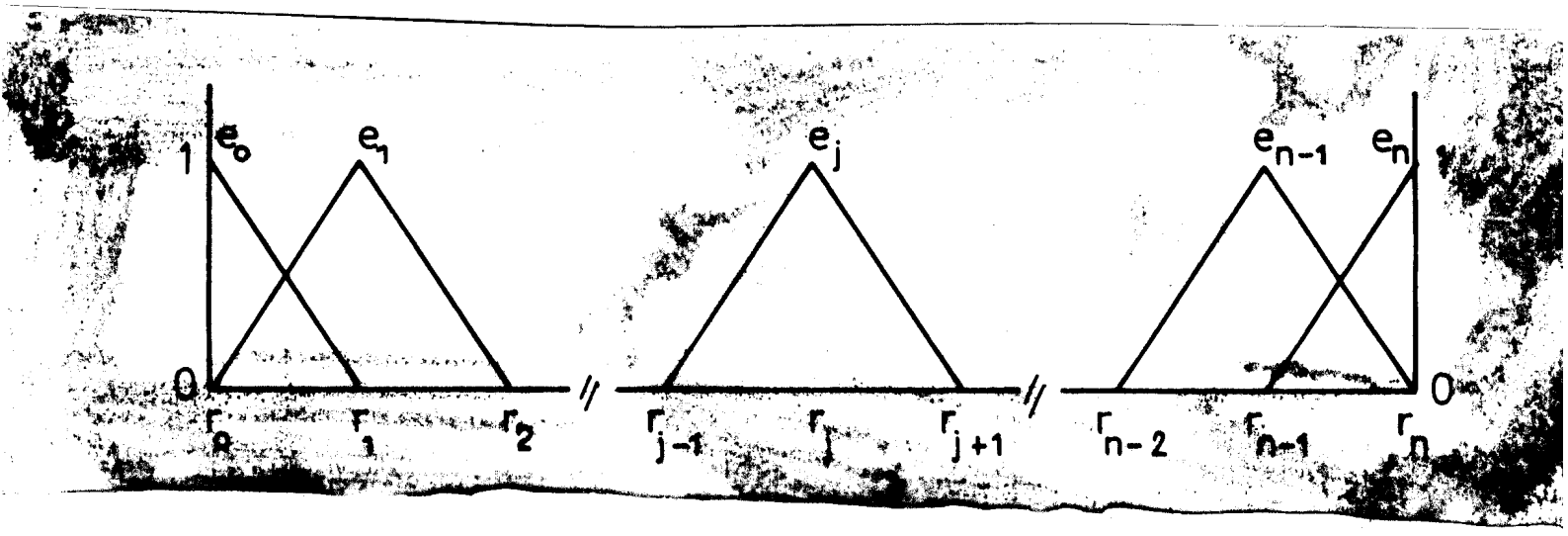

Figure 4: The linear finite elements $e_j(r)$. The three components ξ_r, $i\xi_\theta$, $i\xi_z$ are expanded in terms of these elements.

Fig. 5 shows the eigenfrequency $\omega^2(n)$ as a function of the number of

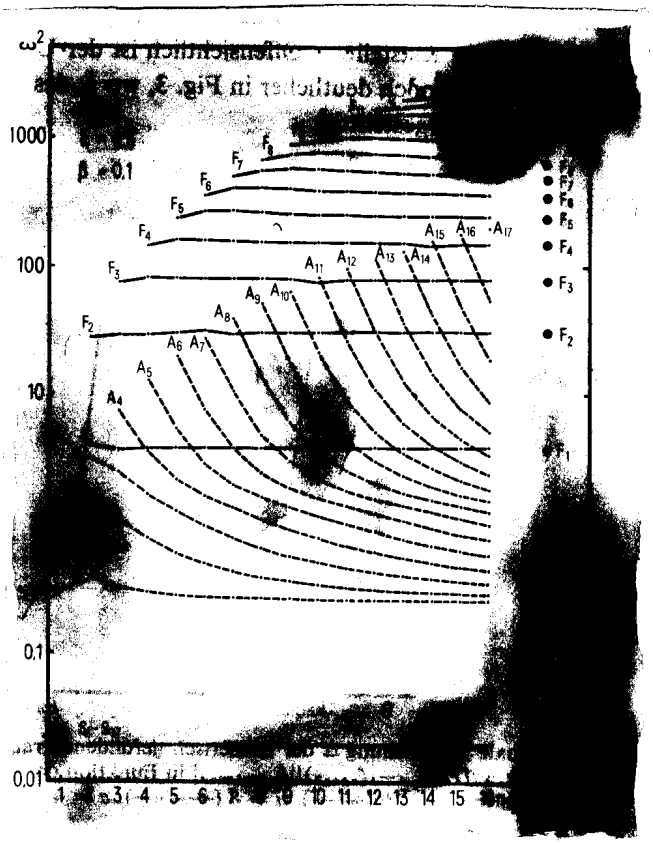

Figure 5: The polluted spectrum ω^2 of the three classes S,A and F as a function of the number of intervals n. Linear elements have been taken for all three vector components. The analytic solution is plotted at the right hand side.

intervals n for k = 0.5, m = 1 and p_o = 0.05. The analytic spectrum given by equations (66) and (70) is given at the right hand side of the figure. The indicies attributed to the different modes denote the number of radial zeros. The numerical results show that the fast wave class (F_1- F_{16}) is obtained with good accuracy. Each of the modes is created near the analytic value and converges quadratically to it. However, the infinitely degenerate Alfvèn class (A_1- A_{17}) spreads out into a discrete spectrum. Each of the radial modes converges again quadratically to the analytic value $\omega^2 = k^2 = 0.25$. However, all the newly created eigenmodes are created with increasingly higher eigenfrequencies. For example, A_{17} created with 16 mesh cells has a greater error than A_{16} created with 15 mesh cells. Note that the "creation curve" of the Alfvèn modes diverges with n^2. The fact that the Alfvèn class spreads out and "pollutes" the fast wave region can be physically visualized as a coupling between the Alfvèn and the fast modes, which leads to badly represented eigenmodes. This effect is largest when the eigenfrequencies of an A and a F mode are close to one another, as for example, A_{11} and F_1 when 14 intervals are used. The same interaction phenomenom occurs within the slow wave class for which the "creation curve" is bounded [29]. But in this case a newly created S mode must cross all the previously created S modes before reaching its correct position in the spectrum.

These results are highly unsatisfactory. A Tokamak-like configuration can be considered as a perturbation of this case by a small axial current. The very strong spreading towards higher values of ω^2 of the Alfvèn modes was precisely why Takeda et al [8] had problems in describing the unstable part of the spectrum. In the next section we show how to get rid of all these problems by an adequate choice of basis functions.

5. Regular Finite Elements

The difficulties encountered in the representation of the Alfvèn class can be understood by examining the contributions of the various terms in eq. (52). The last term vanishes identically since $B_\theta = 0$ in the test case. In the Alfvèn class $D \equiv 0$ and only the first and the third term contribute. With the previous choice of linear finite elements the radial derivative of ξ_r gives a piecewise constant contribution to D, whereas the ξ_θ - contribution is linear. Thus the incompressibility condition $D = 0$ can only be satisfied at one point in the interval. The potential energy then always receives a positive contribution from the second and the fourth term in W_p. This is the cause of the pollution observed in Fig. 5. Thus it is crucial that $D = \underline{\nabla} \cdot \underline{\xi}$ be well represented. Let us first rewrite this quantity in the form

$$\underline{\nabla} \cdot \underline{\xi} = \frac{d\xi_1}{dr} + \xi_2 + k\xi_3 \quad . \tag{73}$$

Here we have performed the variable transformation

$$\hat{\underline{\xi}} = \begin{pmatrix} \xi_1 \\ \xi_2 \\ \xi_3 \end{pmatrix} = U \cdot \underline{\xi} = \begin{pmatrix} 1 & 0 & 0 \\ \frac{1}{r} & \frac{im}{r} & 0 \\ 0 & 0 & i \end{pmatrix} \begin{pmatrix} \xi_r \\ \xi_\theta \\ \xi_z \end{pmatrix} . \tag{74}$$

The essential structure of the variational form, eqs. (26, 47-51) is that it only contains first derivatives d/dr acting on ξ_1 and no derivatives on ξ_2 and ξ_3. In order that the basis functions for the three vector components be "sufficiently regular", we have to take them in a space H where

$$H = H^1(0, r_s) \times L_2(0, r_s) \times L_2(0, r_s) \, , \tag{75}$$

i.e. ξ_1 belongs to the Sobolev space $H^1(0, r_s)$ [39], and ξ_2 and ξ_3 are square integrable.

For the numerical treatment of eq. (26) we need a finite-dimensional (dimension 3 n + 1) space V(V⊂H) of "sufficiently regular" function $\hat{\xi}$. Taking into account the boundary condition for our test case

$$\xi_1 (r_s) = 0 \quad , \tag{76}$$

we find that the space should contain, in the whole range $0 \leq r \leq r_s$, n linearly independent functions $\hat{\xi}$ satisfying eq. (67) and the trivial condition $\xi_3 = 0$. More accurately, V can be defined as described below.

Let V_1 be a finite dimensional subspace of $H^1(0, r_s)$ of type "finite elements" constrained by the boundary condition, eq. (76). Let V_2 and V_3 be two finite-dimensional subspaces of $L_2(0, r_s)$ which have the following properties: for all $\xi_1 \in V_1$ there exists $\xi_2 \in V_2$ and $\xi_3 \in V_3$ such that equation (67) holds. The space is then defined by

$$V = V_1 \times V_2 \times V_3 \quad . \tag{77}$$

From all possible subspaces V, which contain n linearly independent functions satisfying equation (67), we choose the simplest one, that is, the one with a continuous piecewice linear ξ_1 and a piecewise constant ξ_2 and ξ_3 (Fig. 6). In this space of dimension 3 n + 1, $\xi_3 = 0$ and equations (67) and (76) yield 2 n + 1 constraints. Hence n well represented Alfvèn modes may exist. The basis of V is given by

$$\begin{pmatrix} e_j \\ 0 \\ 0 \end{pmatrix}, \; j = 0, 1, \cdots, n \; ; \quad \begin{pmatrix} 0 \\ c_{j+1/2} \\ 0 \end{pmatrix}, \begin{pmatrix} 0 \\ 0 \\ c_{j+1/2} \end{pmatrix}, \; j = 0, \cdots, n-1 \; ; \tag{78}$$

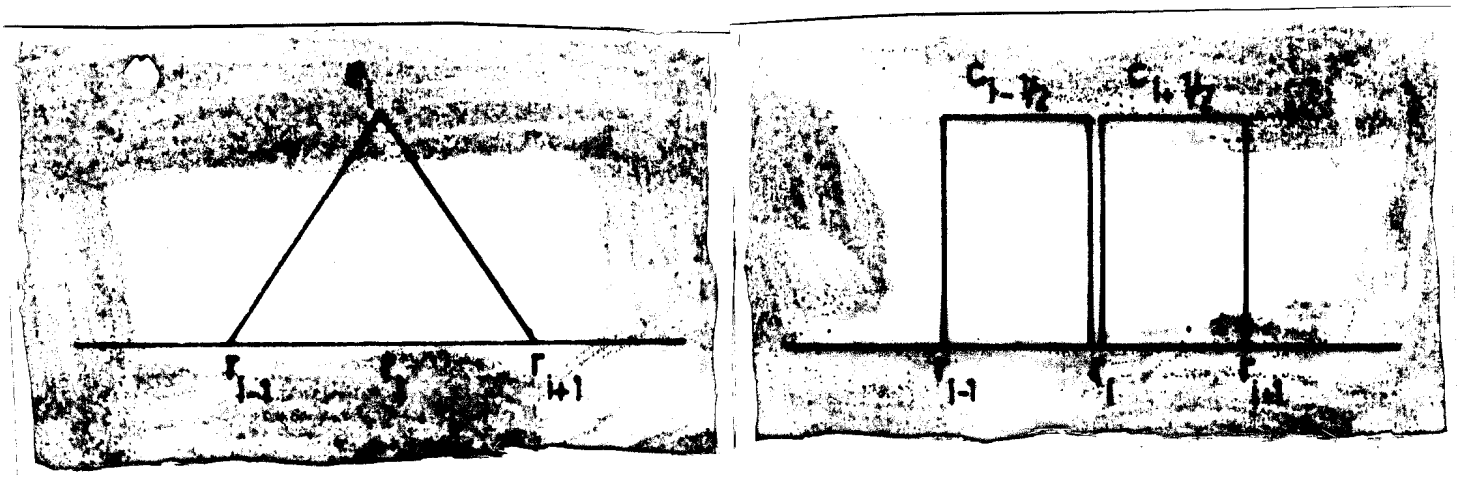

Figure 6: Regular finite elements: $\xi_1 = \xi_r$ is expanded in terms of linear elements $e_j(r)$, (see also Fig. 4), $\xi_2 = (\xi_r + \text{im}\, \xi_\theta)/r$ and $\xi_3 = i\, \xi_z$ are expanded in terms of piecewise constant functions $c_{j+\frac{1}{2}}$. This basis belongs to the class of functions which can satisfies $\nabla \cdot \underset{\sim}{\xi} = d\xi_1/dr + \xi_2 + k\, \xi_3 = 0$.

where e_j are triangular as defined by equation (72) and shown in Fig. 4 and

$$c_{j+\frac{1}{2}}(r) = \begin{cases} 1 & , \quad r_j < r < r_{j+1} \\ 0 & , \quad \text{elsewhere} . \end{cases} \qquad 0 \leq j \leq n-1 \tag{79}$$

The approximation of a displacement $\hat{\underset{\sim}{\xi}}$ in the space V can be written

$$\hat{\underset{\sim}{\xi}} = \sum_{j=0}^{n} \xi_1^j \begin{pmatrix} e_j \\ 0 \\ 0 \end{pmatrix} + \sum_{j=0}^{n-1} \left[\xi_2^{j+\frac{1}{2}} \begin{pmatrix} 0 \\ c_{j+\frac{1}{2}} \\ 0 \end{pmatrix} + \xi_3^{j+\frac{1}{2}} \begin{pmatrix} 0 \\ 0 \\ c_{j+\frac{1}{2}} \end{pmatrix} \right] , \tag{80}$$

where the nodal parameters ξ_1^j, $\xi_2^{j+\frac{1}{2}}$, $\xi_3^{j+\frac{1}{2}}$ are the values of ξ_1 at $r = r_j$ of ξ_2 and ξ_3 at $r = r_{j+\frac{1}{2}} \equiv (r_j + r_{j+1})/2$. The displacement given in eq. (80) is inserted in the variational principle, eq. (26). After all the nodal parameters are varied and the boundary condition (76) fulfilled, an algebraic eigenvalue problem of dimension 3·n results. In the numerical code [20] the integrals that must be carried out in eqs. (48, 49, 52) are performed by a Simpson routine [40] and the eigenvalue problem is solved by a simultaneous inverse vector iteration [41,42].

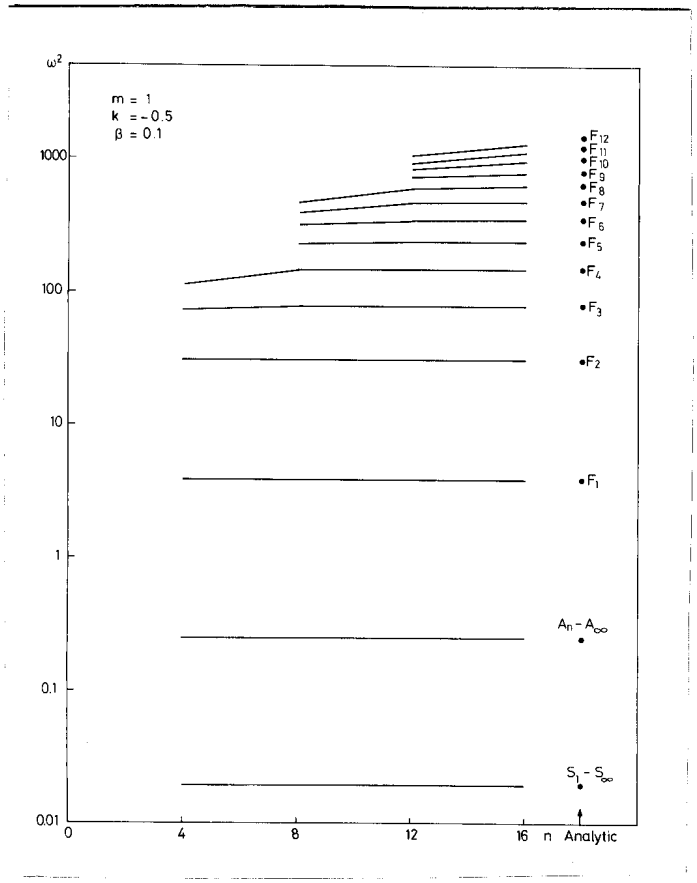

Fig. 7: The "unpolluted" spectrum for the test case obtained with regular finite elements. The three classes S,A and F are shown as a function of the number of intervals n.

Fig. 7 shows the computed spectrum for the same values of parameters as used in Fig. 5. The improvement is striking. There is no more pollution of the degenerate Alfvèn spectrum, and no more pollution of the slow waves. The fast modes are equally well represented. Now, the eigenfunctions are extremely well reproduced [9].

6. Generalization and Applications

In the test case we have used, there is no axial current. When a homogeneous current is progressively switched on, the spectrum undergoes a progressive deformation. The fast modes have a small frequency shift which does not change their character. However, the Alfvèn class undergoes significant transformations. The infinitely degenerate Alfvèn mode spreads into a discrete spectrum with an accumulation point at the upper edge. This accumulation point ω_∞^2, when plotted as a function of the current, describes a parabola with minimum at $\omega^2 = 0$ for a current density j_z given by

$$j_z = -\frac{2kB_z}{m} \qquad (81)$$

With this value for the current the whole Alfvèn class is unstable. The slow waves remain stable but are below the Alfvèn accumulation point. The result is that the whole discrete spectrum becomes contracted as the current approaches the value given in eq. (81) and finally collapses into an infinitely degenerate spectrum $\omega^2 = 0$.

In the general case where the mass density, current density and the magnetic fields have realistic profiles, the dense points of the Alfvèn and the slow wave class open into two stable continua as shown previously in section 2.

When a vacuum region surrounds the plasma column, the boundary condition (76) disappears and the contribution of the vacuum W_v has to be added to the variational principle. This presents no problem since W_v is expressed in terms of ξ_r at the plasma surface. The added degree of freedom results in an additional mode, the "kink".

As an example, Fig. 8 shows the computed m=1 spectrum $\omega^2(k)$ for a screw pinch [43]. The hatched regions are the continua of the Alfvèn (A) and the slow waves (S). The double hatched region indicates that there are two singular surfaces for given q and $\Omega^2 \equiv \omega^2$. As k decreases the frequency of the magneto-acoustic kink mode (M-A Kink) decreases. The kink crosses the two continua, becomes unstable, stable again for $q < 0$ and crosses the two

continua again. The small rectangles in the figure contain the radial components of the displacement vector. This spectrum has been calculated with a general 1-D code named THALIA [20] which uses the regular finite elements. This code has been used in a number of applications:

- Mode Classification [44]
- Belt Pinch [45, 46]
- Alfvèn Heating [43]
- Stabilized Field Pinch [47]

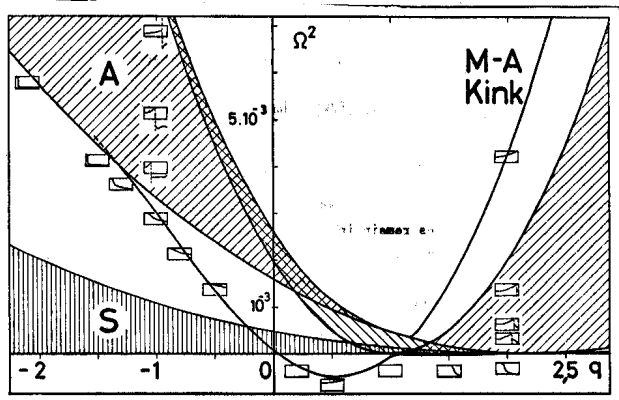

Figure 8: Example of the low frequency part of the m = 1 spectrum of a screw pinch surrounded by a vacuum region. This graph shows the behaviour of the modes as a function of the wave number, $k \equiv q \cdot B_\theta(r_s)/(r_s \cdot B_z(r_s))$. The hatched regions indicate the two continua.

These calculations have revealed the full power of the method. No pollution has been found in all the cases treated which include all kinds of profiles for the mass density, the current density and the magnetic fields. All the features of the spectrum, such as the kinks, the internal kinks, the localized modes, the dense points, the two continua and the stable discrete modes, have been well reproduced in all these applications.

7. Implications

In order to make the transition to the general two-dimensional problem (39), we recall what we consider as the essential features of the one-dimensional case.

The heart of the method is in the choice of different elements for the components of the displacement vector in order to insure the decoupling of the Alfvèn and the fast waves in the limit of no axial current. It turns out that this leads also to the absence of spectral pollution although there is, in general, no obvious correlation between the decoupling and the absence of pollution. The connection between these properties has been investigated by J. Rappaz [22] which provides insight into this question. Since no pollution is observed in all the cases studied, we accept as an empirical result that the two properties are indeed equivalent. This is important for the two-dimensional problem for which there exists no equivalent condition to the Rappaz'condition.

For the general 2-D case we shall proceed by induction, choosing different representations for the components of the displacement vector such that $\underline{\nabla}\cdot\underline{\xi} \equiv 0$ can be satisfied over an extended region. The strongest arguments for such a generalization lies in the similar structure of the W_p contributions to the variational form, eq. (39) and eq. (52). The fact that the marginal modes $\omega^2 = 0$ exactly satisfy $\underline{\nabla}\cdot\underline{\xi} = 0$ constitutes a further evidence of this similarity [3].

There is one difference though in the expressions of δW_p, that is the terms containing F. In the 1-D case F is a numerical factor while it is an operator in the 2-D case. We shall see that this does indeed produce difficulties.

V. THE NON-CIRCULAR STRAIGHT GEOMETRY

1. Reduction to the Non-Circular Straight Geometry

We next consider a more complex problem, namely the case of straight non-circular cross-section geometries (Fig. 9). This case already involves a fully two-dimensional problem, and the transition to the toroidal case is not expected to produce any new difficulties. Our choice is conditionned by the availability of analytic results which we can use to test the basic concepts of the numerical approach.

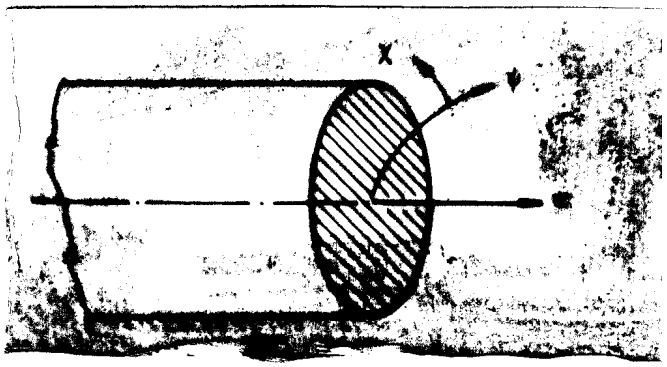

Figure 9: The physical coordinates (ψ, χ, z) in a straight non-circular geometry.

The straight geometry corresponds to a toroidal plasma with an infinite aspect ratio ($r \longrightarrow \infty$). In addition to r, T (eq. 30) and Ψ (eq. 31) also tend to infinity. The new physical equilibrium quantities, the axial magnetic field T/r and the radial coordinate Ψ/r, are both finite. The axial coordinate z is given by $dz = rd\theta$, and the axial wave number k is equal to n/r. Since $r = \infty$, r does not depend on ψ or χ. As a consequence, r = constant can be factored out of the integrals in eqs. (39-42) and cancelled. In other words, the variational form for a straight geometry is identical to that given in eqs. (39-42) when r is set equal to unity and n is replaced by k.

Unlike the cylindrical case the relative phases between X, Y and Z vary in space. This forces us to keep X, Y and Z complex. The arbitrarness of χ is removed by requiring that the Jacobian J be constant on the plasma surface

$$\frac{\partial J(\psi_s, \chi)}{\partial \chi} = 0 . \tag{82}$$

As a result the χ coordinate coincides, on the plasma surface, with the non-orthogonal natural poloidal coordinate used by the Princeton group [28], but everywhere else our coordinate is not the same as that used by the Princeton group. With our choice of orthogonal coordinate system the magnetic axis is a singular point, $J(\chi, 0)$ being indeterminate. For a very elongated cross-section the coordinate system becomes unappropriate in the vicinity of the axis. This is an unavoidable feature of any orthogonal system. We shall limit ourselves to configurations which are not too elongated.

The orthogonal ψ, χ mesh is numbered in such a way that $0 \leq \psi \leq \psi_s$ and $0 \leq \chi \leq 2\pi$. N_ψ and N_χ are the number of intervals in the ψ and χ directions, respectively.

2. The Regular Finite Elements

Performing the transformation (37) $\underline{\nabla} \cdot \underline{\xi}$ becomes

$$\underline{\nabla} \cdot \underline{\xi} = \frac{\partial X}{\partial \psi} + inY + \frac{\partial Z}{\partial \chi} . \tag{83}$$

The variational form (26) contains ψ derivatives acting only on the radial component X. In order that the basis functions for the three vector components be "sufficiently regular" in the domain Ω ($0 \leq \psi \leq \psi_s$, $0 \leq \chi \leq 2\pi$), we take the basis functions in a space U where

$$U = H_0^1(\Omega) \times C_2(\Omega) \times C_2(\Omega) . \tag{84}$$

This signifies that X belongs to the Sobolev space $H_0^1(\Omega)$ [39] and Y and Z to the space $C_2(\Omega)$ defined by (f is either Y or Z)

$$C_2(\Omega) = \left\{ f \in L_2(\Omega) ; \frac{\partial f}{\partial \chi} \in L_2(\Omega) \right\} . \qquad (85)$$

Here $L_2(\Omega)$ denotes the space of square integrable functions.

For the numerical treatment of eq. (26) we need a finite-dimensional space $V \subset U$ defined by

$$V = V_1 \times V_2 \times V_3 . \qquad (86)$$

Here V_1 is a finite dimensional subspace of $H_o^1(\Omega)$ containing the "finite elements". The subspace V_1 is constrained by the boundary condition (43). V_2 and V_3 are two finite dimensional subspaces of $C_2(\Omega)$ which have the following properties: For all $X \in V_1$ there exists $Y \in V_2$ and $Z \in V_3$ such that $\underline{\nabla} \cdot \underline{\xi}$, as expressed in eq. (83), vanishes everywhere.

Among all possible subspaces V, satisfying $\underline{\nabla} \cdot \underline{\xi} = 0$, we choose the most simple one: For X we choose linear basis functions in ψ and χ. We then require that each term in eq. (83) be piecewise constant in ψ and linear in χ. As a result Y and Z are both piecewise constant in ψ. In the χ direction Y varies linearly and Z quadratically.

In a mesh cell the nodal values of X, Y and Z have to be chosen as shown in Fig. 10. Note that there are twice as many values of Z than there are for Y.

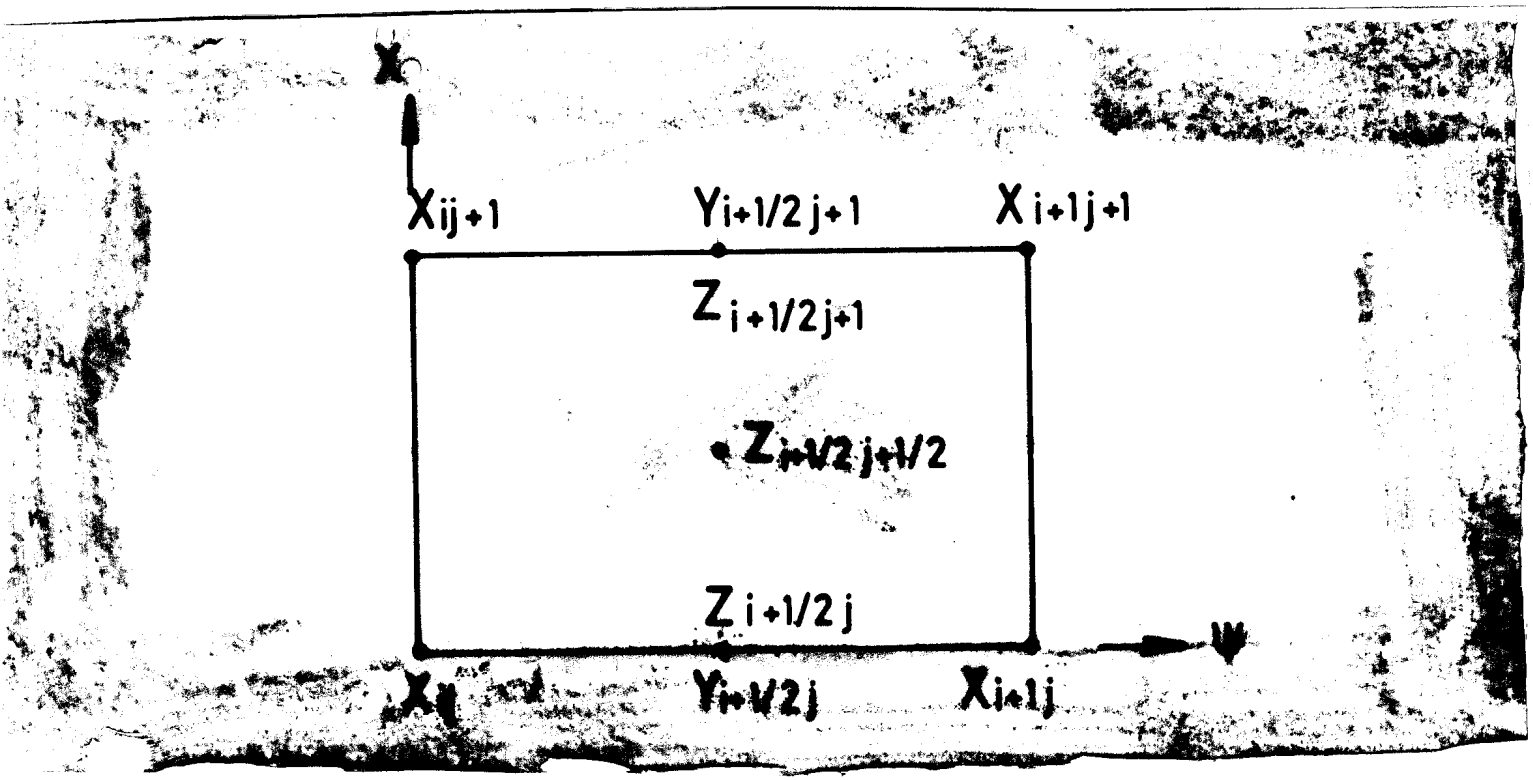

Figure 10: Position of the nodal values in a mesh cell for the regular elements.

The basis for the vector components X and Y become:

$$e_x^{ij} = \left\{ \begin{array}{l} 0 \text{ when } \psi \le \psi_1 \text{ or } \psi \le \psi_{i-1} \text{ or } \chi \le \chi_1 \text{ or } \chi \le \chi_{j-1} \\ \dfrac{\psi-\psi_{i-1}}{\psi_i-\psi_{i-1}} \dfrac{\chi-\chi_{j-1}}{\chi_j-\chi_{j-1}} \text{ when } \psi_{i-1} \le \psi \le \psi_i \text{ and } \chi_{j-1} \le \chi \le \chi_j \\ \dfrac{\psi-\psi_{i-1}}{\psi_i-\psi_{i-1}} \dfrac{\chi-\chi_{j+1}}{\chi_j-\chi_{j+1}} \text{ when } \psi_{i-1} \le \psi \le \psi_i \text{ and } \chi_j \le \chi \le \chi_{j+1} \\ \dfrac{\psi-\psi_{i+1}}{\psi_i-\psi_{i+1}} \dfrac{\chi-\chi_{j-1}}{\chi-\chi_{j-1}} \text{ when } \psi_i \le \psi \le \psi_{i+1} \text{ and } \chi_{j-1} \le \chi \le \chi_j \\ \dfrac{\psi-\psi_{i+1}}{\psi_i-\psi_{i+1}} \dfrac{\chi-\chi_{j+1}}{\chi-\chi_{j+1}} \text{ when } \psi_i \le \psi \le \psi_{i+1} \text{ and } \chi_j \le \chi \le \chi_{j+1} \\ 0 \text{ when } \psi \ge \psi_{N_\psi+1} \text{ or } \psi \ge \psi_{i+1} \text{ or } \chi \ge \chi_{N_\chi+1} \text{ or } \chi \ge \chi_{j+1} \end{array} \right\} \quad (87)$$

$$e_y^{i+\frac{1}{2}j} = \left\{ \begin{array}{l} 0 \text{ when } \psi < \psi_i \text{ or } \chi \leq \chi_1 \text{ or } \chi \leq \chi_{j-1} \\ \dfrac{\chi - \chi_{j-1}}{\chi_j - \chi_{j-1}} \text{ when } \psi_i < \psi < \psi_{i+1} \text{ and } \chi_{j-1} \leq \chi \leq \chi_j \\ \dfrac{\chi - \chi_{j+1}}{\chi_j - \chi_{j+1}} \text{ when } \psi_i < \psi < \psi_{i+1} \text{ and } \chi_j \leq \chi \leq \chi_{j+1} \\ 0 \text{ when } \psi > \psi_{i+1} \text{ or } \chi \geq \chi_{N_\chi+1} \text{ or } \chi \geq \chi_{j+1} \end{array} \right\} . \qquad (88)$$

For the vector component Z we need two quadratic basis functions, e_{Z_1} and e_{Z_2}, given by

$$e_{z_1}^{i+\frac{1}{2}j} = \left\{ \begin{array}{l} 0 \text{ when } \psi < \psi_i \text{ or } \chi < \chi_1 \text{ or } \chi < \chi_{j-1} \\ \dfrac{2(\chi - \chi_{j-1})(\chi - \chi_{j-\frac{1}{2}})}{(\chi - \chi_{j-1})^2} \text{ when } \psi_i < \psi < \psi_{i+1} \text{ and } \chi_{j-1} \leq \chi \leq \chi_j \\ \dfrac{2(\chi - \chi_{j+1})(\chi - \chi_{j+\frac{1}{2}})}{(\chi - \chi_{j+1})^2} \text{ when } \psi_i < \psi < \psi_{i+1} \text{ and } \chi_j \leq \chi \leq \chi_{j+1} \\ 0 \text{ when } \psi > \psi_{i+1} \text{ or } \chi > \chi_{N_\chi+1} \text{ or } \chi > \chi_{j+1} \end{array} \right\} \qquad (89)$$

$$e_{z_2}^{i+\frac{1}{2}\,j+\frac{1}{2}} = \begin{cases} 0 \text{ when } \psi < \psi_i \text{ or } \chi < \chi_j \\ \dfrac{4\,(\chi-\chi_j)(\chi-\chi_{j+1})}{(\chi-\chi_j)^2} \text{ when } \psi_i < \psi < \psi_{i+1} \text{ and } \chi_j \leq \chi \leq \chi_{j+1} \\ 0 \text{ when } \psi > \psi_{i+1} \text{ and } \chi > \chi_{j+1} \end{cases} \quad (89)$$

The elements are shown in Fig. 11. Note that e_x^{ij} has a support extending over 4 mesh cells, $e_y^{i+\frac{1}{2}j}$ and $e_{z_1}^{i+\frac{1}{2}j}$ are non-zero in two mesh cells while $e_{z_2}^{i+\frac{1}{2}j+\frac{1}{2}}$ gives an integral contribution in only one mesh cell. The transformed total displacement $\hat{\underset{\sim}{\xi}}_n$ (eq. 38) can then be written:

$$\begin{aligned} \hat{\underset{\sim}{\xi}}_n(\psi,\chi) = & \sum_{i=0}^{N_\psi}\sum_{j=0}^{N_\chi} X_{ij}\, e_x^{ij} + \\ & + \sum_{i=0}^{N_\psi-1}\sum_{j=0}^{N_\chi} Y_{i+\frac{1}{2}\,j}\, e_y^{i+\frac{1}{2}\,j} + \\ & + \sum_{i=0}^{N_\psi-1}\sum_{j=0}^{N_\chi} Z_{i+\frac{1}{2}\,j}\, e_{z_1}^{i+\frac{1}{2}\,j} + \\ & + \sum_{i=0}^{N_\psi-1}\sum_{j=0}^{N_\chi-1} Z_{i+\frac{1}{2}\,j+\frac{1}{2}}\, e_{z_2}^{i+\frac{1}{2}\,j+\frac{1}{2}} . \end{aligned} \quad (90)$$

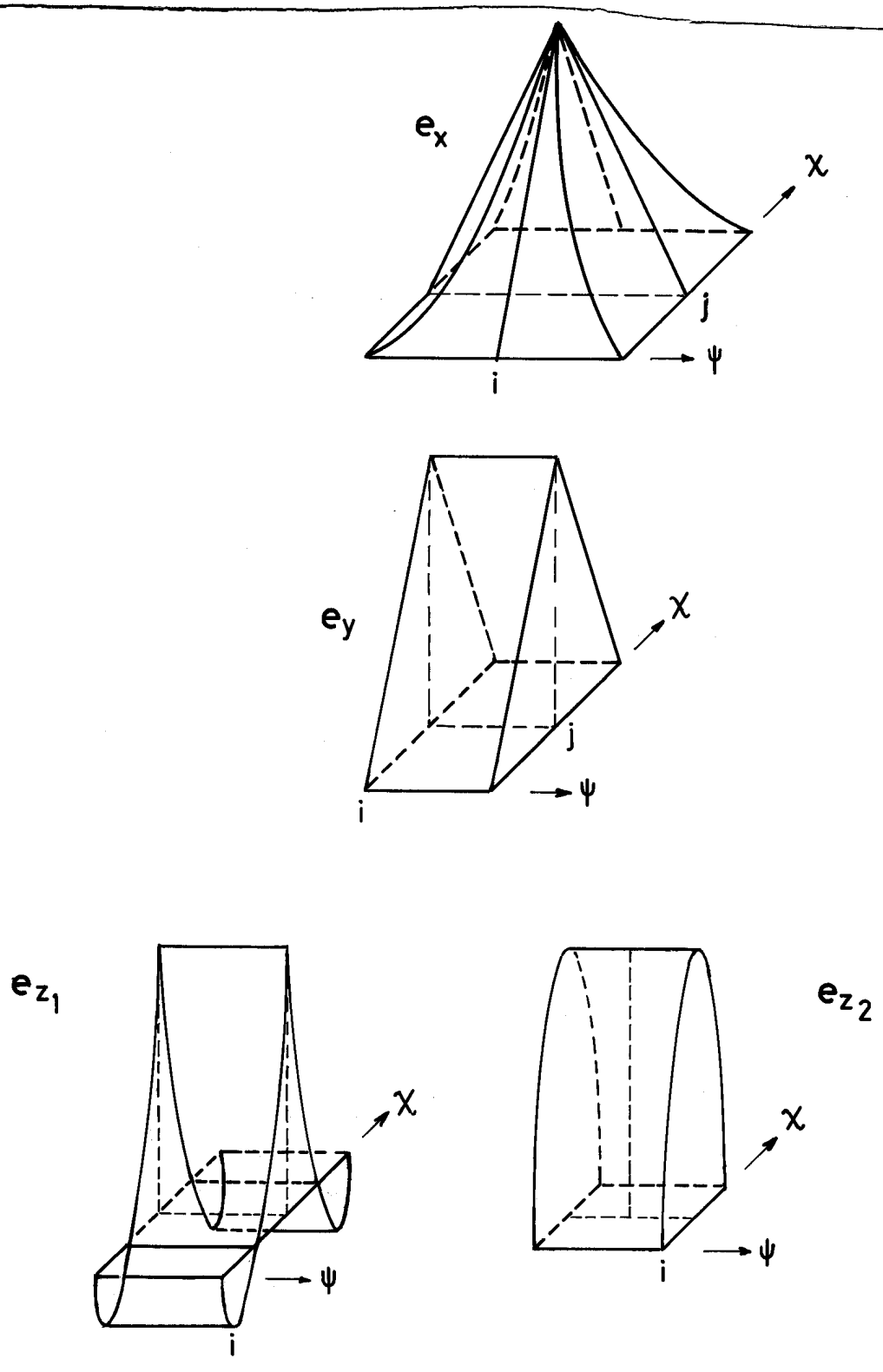

Figure 11: Shape of the regular basis functions. The maximum heights of e_x, e_y, e_{z_1} and e_{z_2} are 1.

The regularity condition given in eq. (43) requires in this expansion that

$$X_{0j} = 0 \quad . \tag{91}$$

For a wall constrained plasma, the boundary condition, eq. (44), becomes

$$X_{N_\psi j} = 0 \quad . \tag{92}$$

The periodicity in χ implies the relations

$$\begin{aligned} X_{i\,N_\chi} &= X_{i\,0} \\ Y_{i+1/2\,N_\chi} &= Y_{i+1/2\,0} \\ Z_{i+1/2\,N_\chi} &= Z_{i+1/2\,0} \quad . \end{aligned} \tag{93}$$

A code has been written which solves the variational problem (26) by using the expansion in eq. (90). In order to verify the applicability of this approach, we solve some simple test problems for which reliable results are known.

3. The Circular Test Case

As a first test we choose the same cylindrical configuration as in the 1-D test case, but with an additional constant axial current density $j_z = J_z T/r_s$. We shall consider two cases: A plasma column surrounded by a conducting shell at a radius $r_w = 2\ r_s$, and a wall constrained plasma. In both cases we choose a current density $J_z = 0.4$ and investigate the $m = 1$ modes. We are interested in the unstable part of the spectrum.

The results for the plasma with a conducting shell are shown in Fig. 12. The solid curves have been calculated with the 1-D code. The fastest

growing mode is the kink. The other modes around q = 1 are internal modes characterized by a small displacement of the plasma surface. As mentionned in section IV.6, for q = 1, the marginal point $\Gamma^2 = -\omega^2 = 0$ is the accumulation point of the Alfvèn class. Thus there are an infinite number

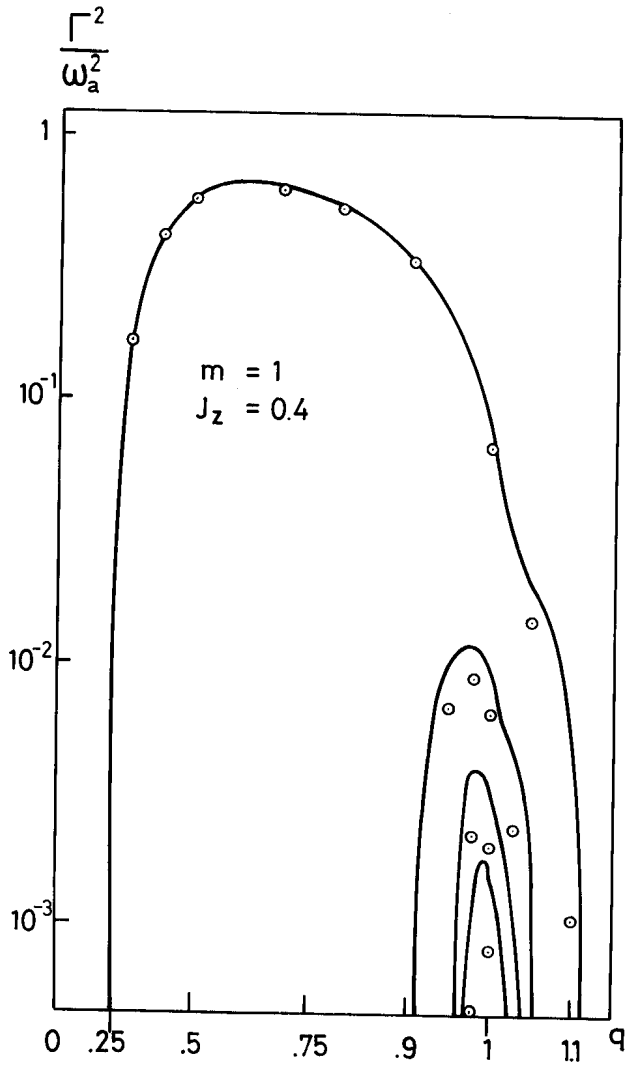

Figure 12: The circular plasma test case with a vacuum region. $\Gamma^2 \equiv -\omega^2$ has the same normalization as ω^2 in the 1-D test case. The solid curves represent the 1-D calculations. The dotted circles indicate the results of calculations performed with our 2-D code using regular finite elements.

of unstable modes when q = 1. With the 1-D numerical code one obtains N_ψ unstable values for q = 1 which is the maximum number that can be found with N_ψ intervals in ψ direction. Note that the growth rate $\Gamma = -i\omega$ of the kink is one order of magnitude larger than the second fundamental mode. The small circles in Fig. 12 represent the results of the 2-D code. Because of the symmetry, it was possible to treat only half the range in χ, namely $0 \leq \chi \leq \pi$, which shortened the size of the computation. The results correspond to $N_\psi = 12$ and $N_\chi = 24$. We see that the kink mode is well reproduced. Results obtained for the internal modes, around q = 1, are qualitatively correct but an appreciable discrepancy remains. The growth rates of these modes are of the order of 10^{-2} and less. This is two orders of magnitude smaller than the typical eigenfrequencies of the fast modes. This confirms the good decoupling between the Alfvèn and the fast waves. The discrepancy becomes worse, though, as m is increased. For example, with the same parameters as taken for Fig. 12, it is impossible to obtain the m = 2 unstable internal modes even when calculating with $N_\chi = 40$. This justifies examining internal modes more closely.

The second case, shown in Fig. 13, shows a convergence study of the fundamental m = 1 internal mode for the case of a wall constrained plasma. We

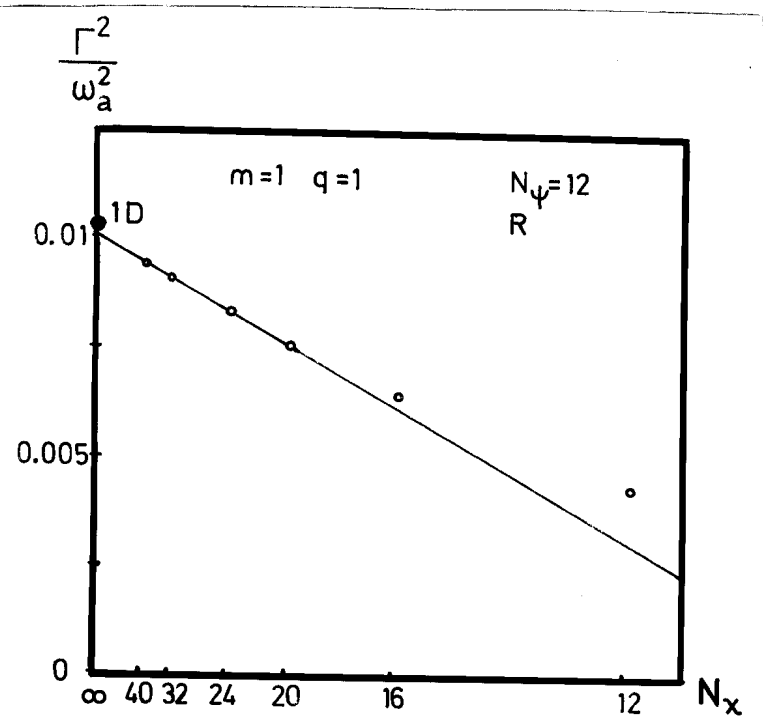

Fig. 13: Convergence study for regular elements (R). The growth rate squared Γ^2 is plotted versus $1/N_\chi^2$ for a wall constrained constant current carrying screw pinch. The solid straight line corresponds to a quadratic convergence.

fix q = 1. Treating the wall constrained plasma, it was possible to use a larger number of mesh points. The essential feature, however, does not change. In Fig. 13 $\Gamma^2 = -\omega^2$ is represented as a function of $1/N_\chi^2$. Note that N_χ represents here the number of azimuthal intervals in half the range, namely $0 \leq \chi \leq \pi$. The straight line corresponds to a quadratic convergence. We recognize that there is, in fact, quadratic convergence, but only for $N_\chi \geq 10$. With fewer intervals the results are closer to the correct value than predicted by the quadratic convergence line. In principle, knowing the convergence behaviour of the method, it is possible to extrapolate to $N_\chi = \infty$. Unhappily in more complicated cases, for example for $m \geq 2$ or in an elongated cross-section, the number of points beyond which the convergence is indeed quadratic becomes unacceptably high.

We may then conclude that the kink modes are well reproduced with this method but that the problem with the weakly growing internal modes remains unsolved. In chapter VI a new method is proposed which removes these difficulties.

4. The Elliptical Test Case

To test the effect of non-circularity we choose an equilibrium proposed by Gajewski [48] which has an elliptical cross-section and a constant current density j_z. The axial magnetic field T and the mass density ρ also are taken to be homogeneous. The elliptical plasma surface is defined by the minor radius of the plasma a, and the eccentricity of the ellipse, $\varepsilon = b/a$ where b is the major plasma radius. We assume a vacuum region around the plasma and a confocal conducting wall enclosing the elliptical plasma and the vacuum region.

The surfaces of constant magnetic flux $\Psi(r,z)$ are concentric ellipses

$$\Psi(r,z) = \Psi_s \left(r^2 + z^2/\varepsilon^2 \right) , \tag{94}$$

with $\Psi_s = \frac{\varepsilon^2 j_z}{2(\varepsilon^2+1)}$. The poloidal field B becomes

$$B(r,z) = 2\Psi_s \left(r^2 + z^2/\varepsilon^4\right)^{1/2} . \tag{95}$$

The location of the conducting shell is given by

$$\left(\frac{r}{\mathcal{A}}\right)^2 + \left(\frac{z}{\mathcal{B}}\right)^2 = 1 \tag{96}$$

where

$$\mathcal{A} = a\left\{\frac{1-\varepsilon^2+\left[(1+\varepsilon^2)^2+4\varepsilon^2(r_w^4-1)\right]^{1/2}}{2}\right\}^{1/2}$$
$$\mathcal{B} = r_w/\mathcal{A} . \tag{97}$$

r_w^2 is the ratio of the crossectional area of the shell to the crossectional area of the plasma.

The orthogonal coordinate χ is defined by

$$\left(\frac{z}{\varepsilon a \sin\chi}\right)^{\varepsilon^2} = \frac{r}{a\cos\chi} . \tag{98}$$

The plasma surface corresponds to $z = \varepsilon a \sin\chi$ and $r = a\cos\chi$ which verifies that χ coincides there with the angular coordinate chosen by Dewar et al [26]. For all other values of $\Psi \neq \Psi_s$ they naturally differ. The Jacobian J is then given in semi-implicit form by

$$J = 2\frac{\varepsilon^2+1}{j_z}\,\frac{rz}{\sin 2\chi}\,\frac{\varepsilon^2\cos^2\chi + \sin^2\chi}{r^2\varepsilon^4 + z^2} . \tag{99}$$

On the plasma surface $J = (\varepsilon^2+1)/(\varepsilon j_z)$.

Dewar et al [26] were able to solve exactly for the spectrum in what is usually called the "kink ordering", namely in the limit $B_\theta/T \sim ka \ll 1$. They showed that, in this order, only the kink mode can become unstable with a

growth rate which scales as ka. The internal modes remain stable.

The modes can be divided into classes which are the analogue of the separation in azimuthal numbers m in the circular case. We are interested in the kink mode which becomes the m = 1 kink in the circular limit. Introducing the quantities

$$\begin{aligned} \omega_a^2 &= \varepsilon^2 j_z^2 / \beta (1+\varepsilon^2)^2 \\ A_1 &= (1+\varepsilon^2)(1+q^2)/2\varepsilon \\ A_2 &= 1-q^2 \\ q &= k(1+\varepsilon^2)T/\varepsilon j_z \ , \end{aligned} \tag{100}$$

we find that the growth rate for $r_v = \infty$ is given by

$$\Gamma^2(q) = \omega_a^2 \sqrt{A_1 - A_2}\left(\sqrt{A_1 + A_2} - \sqrt{A_1 - A_2}\right) . \tag{101}$$

We have computed this analytically treatable case with our 2-D code, choosing a current density of $j_z = 0.05$. This current density should be sufficiently small in order that the kink approximation be valid. For numerical reasons it is not possible to solve the case with $r_w = \infty$. The crosses and the circles in Fig. 14 correspond to calculations performed with $r_w = 20$, $N_\psi = 14$ and $N_\chi = 32$. As in the previous section the symmetry allows us to treat only half the interval, $0 \leq \chi \leq \pi$, but for clarity we give the value of N_χ for the whole range $0 \leq \chi \leq 2\pi$. The small circles indicate the numerical results for the elliptical case. The elliptical results only fit the analytical curve in the short wavelength region which suggests that the conducting wall has an important stabilizing effect on the long wavelength modes. In order to check the results we made a convergence study for different values of r_w, choosing q = 0.1. Three values of r_w, namely 10, 20 and 40, have been used. One recognizes that Γ^2 varies linearly with the inverse of r_w. The extrapolation to $r_w = \infty$ is shown by a

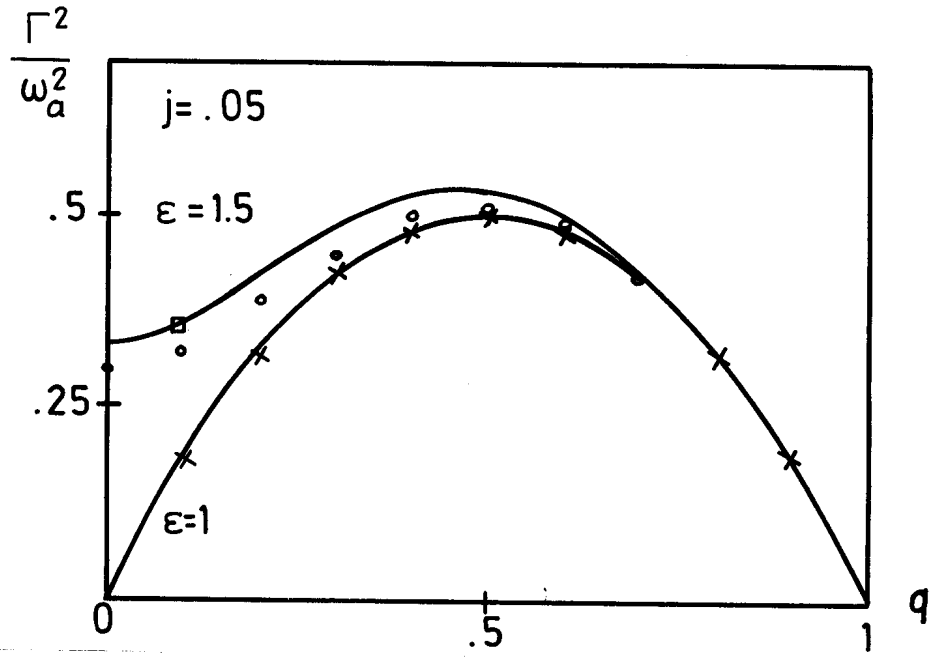

Figure 14: Comparison of the calculated and analytic values of the growth rates for the "m = 1" external kink. The calculated values are obtained with $r_w = 20$ and the analytical results with $r_w = \infty$. Analytic results (indicated by solid lines) are given for a circle and for an ellipse, $\varepsilon = 1.5$. The square at q = 0.1 on the $\varepsilon = 1.5$ curve shows the extrapolated value for $r_w = \infty$ and is obtained from a convergence study.

small square in Fig. 14. This result agrees with the analytic result and thus confirms that the discrepancy is due to our choice of r_w.

We conclude that this code, which uses regular finite elements, reproduces well the kink modes even in the low beta limit.

5. Application to an Elliptical Screw-Pinch

In Fig. 12 we have plotted the unstable part of the spectrum of the m = 1 mode for the circular test case. As an application of our code, we compute the effect of an ellipticity on this spectrum. We use the same equilibrium and definitions as in the previous section. We choose a current $j_z = 0.4$ T/a which is sufficiently strong to allow a simultaneous representation of the kink and the internal modes on the same graph. The conducting shell has

been placed at $r_w = 2$. Figure 15 shows the results obtained. We represent the square of the normalized growth rate $\Gamma^2(q) \equiv -\frac{\omega^2 a^2 \rho}{T^2}\left(\frac{1+\varepsilon^2}{2\varepsilon}\right)^2$ as a function of q defined in eqs. (100). The solid lines represent the 1-D results for the circular case and the dotted circles those for an

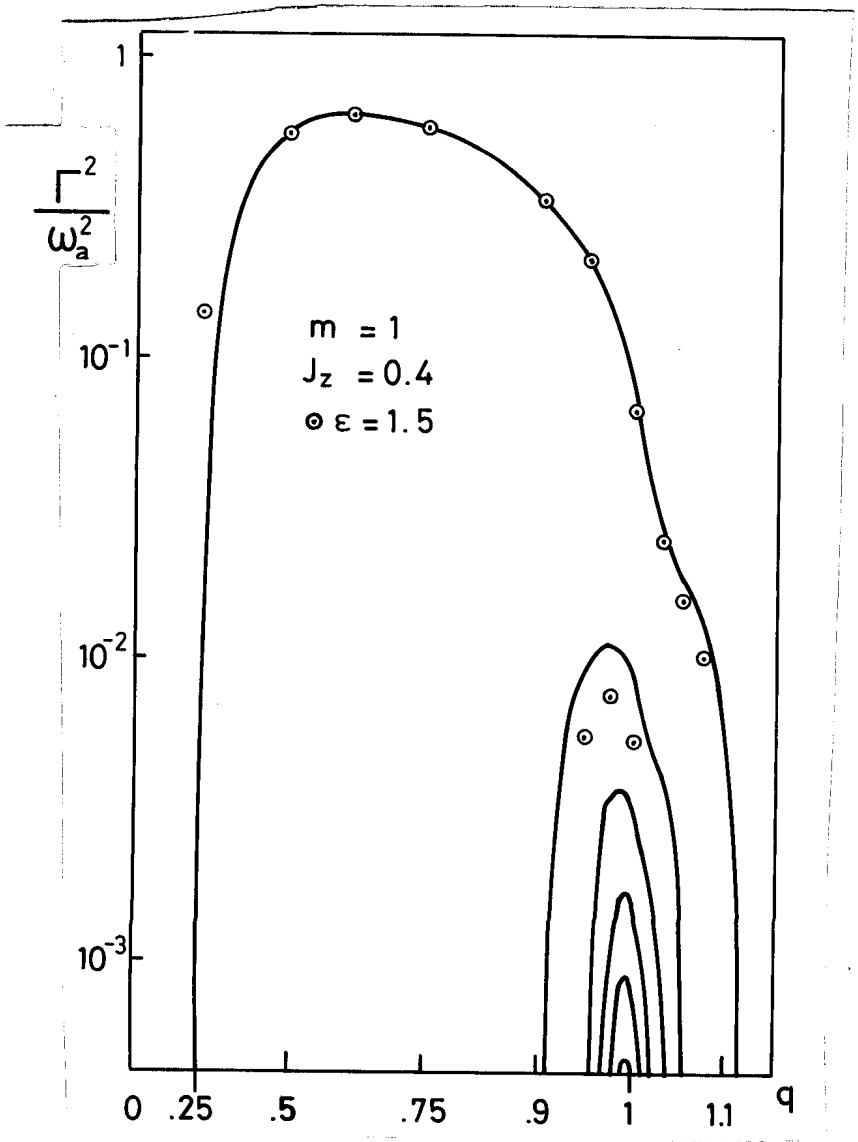

Figure 15: Unstable part of the spectrum in a straight geometry with homogeneous current and mass densities and a constant axial magnetic field. The conducting shell is situated at $r_w = 2.0$. The solid lines represent the different fundamental modes for the circular case. The dotted circles are normalized results for an ellipticity of $\varepsilon = 1.5$ and calculated with our 2-D code using regular finite elements. Note the strong stabilization of the elliptical internal modes around q = 1.

ellipticity of $\varepsilon = 1.5$. Each point has been obtained by a convergence study analogous to Fig. 13, using 12, 16 and 20 azimuthal intervals.

We see that the long wavelength modes are destabilized by the ellipticity. The modes around q = 1 appear to be stabilized by the ellipticity. Laval [12] has shown that this cannot be correct. In fact, with the number of mesh points taken, no clear convergence law has emerged yet, and an assumed quadratic convergence underestimates the final value. From a practical point of view, it is not worthwhile to take more intervals. If the code is to be a powerful tool in calculating unstable displacements for realistic configurations, it is necessary that not too large a number of intervals be required. Typically, one should not take more than 40 azimuthal intervals.

In conclusion this 2-D code has some of the interesting features already found in the 1-D case. No spectral pollution has been observed. The kinks are well reproduced even in the low-β limit. However, the reproduction of the weakly growing modes remains a problem. These internal modes, lying around q = 1, are characterized by an almost vanishing contribution from the FX, FY and FZ terms. With the regular finite elements the two contributions to these terms have different functional dependence in χ. We are confronted with a similar situation as in the 1-D case with $\underline{\nabla} \cdot \underline{\xi}$, when the same hat functions were used for all three components of $\underline{\xi}$. FX, for example, cannot vanish identically over a cell and the first term, $|FX|^2$, in eq. (39), gives then a positive contribution to W_p. This leads to a coupling between members of the Alfvèn class which stabilizes the unstable internal modes. In the next chapter we propose a method which removes this last difficulty.

VI. THE FINITE HYBRID ELEMENTS

1. "Finite Differences Description" of the Lowest Order Finite Hybrid Elements

We have seen in the preceeding calculations with regular finite elements that a coupling between different Alfvèn modes gives rise to a stabilizing effect. This stabilization becomes visible only when one looks for weakly growing modes. This was the case when we treated the internal modes. The aim of this chapter is to propose a method where the coupling effect disappears. The coupling effect results because in a mesh cell there are different variations of the various quadratic terms in W_p. We propose a kind of finite differences applied to the variational principle which we call "finite hybrid elements". In this method the functions have the same functional dependence as their derivatives. We can then obtain a numerical formulation of the variational principle in which all the quadratic terms have the same functional dependence, neglecting the variation of the equilibrium quantities in a mesh cell. In our case all quadratic terms will be piecewise constant in each mesh cell. We expect that the stabilizing couplings will then be essentially removed.

In order to be able to give a simple "finite differences formulation" of the hybrid elements we define in Fig. 16 the position of the unknowns in a mesh cell. The nodal values of the vector component X are defined at the mesh points; whereas, the other two components, Y and Z, are defined at the middle of the ψ- intervals. We introduce the lowest order hybrid elements by a calculation prescription which corresponds to a centred finite difference scheme. Function values and all derivatives are expressed at the mid points of each mesh cell in the integration, the functional values and derivatives are taken to be constant over the whole mesh cell:

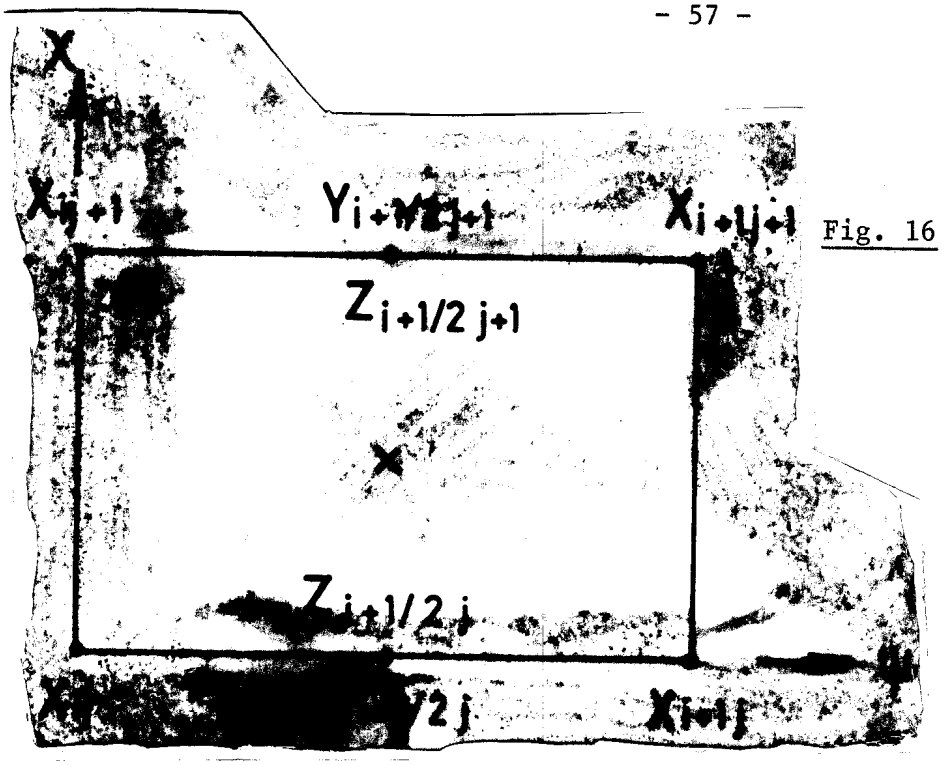

Fig. 16: Position of the nodal values in a mesh cell for the "finite differences description" of the finite hybrid elements.

$$X_{i+\frac{1}{2}\,j+\frac{1}{2}} = \frac{X_{ij} + X_{i+1\,j} + X_{i\,j+1} + X_{i+1\,j+1}}{4}$$

$$Y_{i+\frac{1}{2}\,j+\frac{1}{2}} = \frac{Y_{i+\frac{1}{2}\,j} + Y_{i+\frac{1}{2}\,j+1}}{2} \qquad (102)$$

$$Z_{i+\frac{1}{2}\,j+\frac{1}{2}} = \frac{Z_{i+\frac{1}{2}\,j} + Z_{i+\frac{1}{2}\,j+1}}{2}$$

$$\left(\frac{\partial X}{\partial x}\right)_{i+\frac{1}{2}\,j+\frac{1}{2}} = \frac{(X_{i\,j+1} + X_{i+1\,j+1}) - (X_{ij} + X_{i+1\,j})}{2\,(x_{j+1} - x_j)}$$

$$\left(\frac{\partial Y}{\partial x}\right)_{i+\frac{1}{2}\,j+\frac{1}{2}} = \frac{Y_{i+\frac{1}{2}\,j+1} - Y_{i+\frac{1}{2}\,j}}{x_{j+1} - x_j} \qquad (103)$$

$$\left(\frac{\partial Z}{\partial x}\right)_{i+\frac{1}{2}\,j+\frac{1}{2}} = \frac{Z_{i+\frac{1}{2}\,j+1} - Z_{i+\frac{1}{2}\,j}}{x_{j+1} - x_j}$$

$$\left(\frac{\partial X}{\partial \psi}\right)_{i+\frac{1}{2}\,j+\frac{1}{2}} = \frac{(X_{i+1\,j} + X_{i+1\,j+1}) - (X_{ij} + X_{i\,j+1})}{2\,(\psi_{i+1} - \psi_i)} \qquad (104)$$

This approach is similar to that proposed by E. Stiefel [49] to solve the Laplace equation.

The expressions for the values of the function given by eqs. (102), of their derivatives (eqs. 103) and of the Ψ- derivative acting on X (eq. 104), are introduced into the variational form (eq. 26) which becomes

$$\delta L = \sum_i \int_{\Psi_i}^{\Psi_{i+1}} d\Psi \sum_j \int_{\chi_j}^{\chi_{j+1}} d\chi \, \frac{1}{J} \{I\} = 0 \qquad (105)$$

where

$$\begin{aligned}
\{I\} = {} & \frac{1}{B^2 r^2} \left| \frac{1}{J} \left(\frac{\partial X}{\partial \chi}\right)_{i+\frac{1}{2} j+\frac{1}{2}} + X_{i+\frac{1}{2} j+\frac{1}{2}} \left(\frac{\partial \frac{1}{J}}{\partial \chi} + \frac{in T}{r^2} \right) \right|^2 + \\
& + \frac{T^2}{r^2} \left| \left(\frac{\partial X}{\partial \psi}\right)_{i+\frac{1}{2} j+\frac{1}{2}} + r^2 X_{i+\frac{1}{2} j+\frac{1}{2}} \frac{\partial \frac{1}{r^2}}{\partial \psi} - \frac{1}{J} \left(\frac{\partial Y}{\partial \chi}\right)_{i+\frac{1}{2} j+\frac{1}{2}} - \right. \\
& \left. - Y_{i+\frac{1}{2} j+\frac{1}{2}} \frac{\partial \frac{1}{J}}{\partial \chi} + \left(\frac{\partial Z}{\partial \chi}\right)_{i+\frac{1}{2} j+\frac{1}{2}} + r^2 Z_{i+\frac{1}{2} j+\frac{1}{2}} \frac{\partial \frac{1}{r^2}}{\partial \chi} \right|^2 + \\
& + B^2 \left| \left(\frac{\partial X}{\partial \psi}\right)_{i+\frac{1}{2} j+\frac{1}{2}} + X_{i+\frac{1}{2} j+\frac{1}{2}} \left(J \frac{\partial \frac{1}{J}}{\partial \psi} + \frac{j}{B^2 r} \right) + in Y_{i+\frac{1}{2} j+\frac{1}{2}} - \right. \\
& \left. - \frac{in J T}{r^2} Z_{i+\frac{1}{2} j+\frac{1}{2}} \right|^2 + \\
& + \gamma p_0 \left| \left(\frac{\partial X}{\partial \psi}\right)_{i+\frac{1}{2} j+\frac{1}{2}} + in Y_{i+\frac{1}{2} j+\frac{1}{2}} + \left(\frac{\partial Z}{\partial \chi}\right)_{i+\frac{1}{2} j+\frac{1}{2}} \right|^2 - 2 \frac{K}{J} \left| X_{i+\frac{1}{2} j+\frac{1}{2}} \right|^2 - \\
& - \omega^2 \rho_0 \left[\frac{1}{Br^2} \left| X_{i+\frac{1}{2} j+\frac{1}{2}} \right|^2 + r^2 \left| Y_{i+\frac{1}{2} j+\frac{1}{2}} \right|^2 + J^2 B^2 \left| Z_{i+\frac{1}{2} j+\frac{1}{2}} \right|^2 \right] .
\end{aligned} \qquad (106)$$

The variation will be performed on the real and imaginary parts of the nodal values shown in Fig. 16. In eq. (105) the contribution of the vacuum is omitted since we shall consider here only the wall constrained case. The regularity and the boundary condition (eqs. 43 and 44) become

$$\begin{aligned} X_{0j} &= 0 \\ & \qquad\qquad 0 \le j \le N_\chi \\ X_{N_\psi j} &= 0 \,. \end{aligned} \tag{107}$$

The periodicity conditions in χ give

$$\begin{aligned} X_{i+\frac{1}{2}\,0} &= X_{i+\frac{1}{2}\,N_\chi} \\ Y_{i+\frac{1}{2}\,0} &= Y_{i+\frac{1}{2}\,N_\chi} \qquad\qquad 0 \le i \le N_\psi \\ Z_{i+\frac{1}{2}\,0} &= Z_{i+\frac{1}{2}\,N_\chi} \,. \end{aligned} \tag{108}$$

In the next section we represent a more general finite element formulation from which the above results can be recovered as a special case.

2. "Finite Element Description" of the Lowest Order Finite Hybrid Elements

The Lagrangian given by eqs. (26, 39-42) can be rewritten in a completely equivalent form:

$$
\begin{aligned}
\delta L = \delta \iint d\psi\, d\chi\, \frac{1}{J} \Bigg\{ & \frac{1}{B^2 r^2} \left| \frac{1}{J} \frac{\partial X^{(1)}}{\partial \chi} + X^{(2)} \left(\frac{\partial \frac{1}{J}}{\partial \chi} + \frac{in T}{r^2} \right) \right|^2 + \\
& + \frac{T^2}{r^2} \left| \frac{\partial X^{(3)}}{\partial \psi} + r^2 X^{(2)} \frac{\partial \frac{1}{r^2}}{\partial \psi} - \frac{1}{J} \frac{\partial Y^{(1)}}{\partial \chi} - Y^{(2)} \frac{\partial \frac{1}{J}}{\partial \chi} + \frac{\partial Z^{(1)}}{\partial \chi} + r^2 Z^{(2)} \frac{\partial \frac{1}{r^2}}{\partial \chi} \right|^2 + \\
& + B^2 \left| \frac{\partial X^{(3)}}{\partial \psi} + X^{(2)} \left(J \frac{\partial \frac{1}{J}}{\partial \psi} + \frac{j}{B^2 r} \right) + in Y^{(2)} - \frac{in JT}{r^2} Z^{(2)} \right|^2 + \\
& + \gamma p_0 \left| \frac{\partial X^{(3)}}{\partial \psi} + in Y^{(2)} + \frac{\partial Z^{(1)}}{\partial \chi} \right|^2 - 2 \frac{K}{J} \left| X^{(2)} \right|^2 \Bigg\} + \\
& + \delta \iint d\chi\, d\chi'\, G_s(\chi|\chi') \left[\frac{1}{J} \frac{\partial X^{(1)}}{\partial \chi} + X^{(2)} \left(\frac{\partial \frac{1}{J}}{\partial \chi} + \frac{in T}{r^2} \right) \right]_{\chi} \left[\frac{1}{J} \frac{\partial X^{(1)}}{\partial \chi} + X^{(2)} \left(\frac{\partial \frac{1}{J}}{\partial \chi} + \frac{in T}{r^2} \right) \right]^*_{\chi'} - \\
& - \delta \omega^2 \iint d\psi\, d\chi\, \rho_0 \frac{1}{J} \left[\frac{\left| X^{(2)} \right|^2}{B^2 r^2} + r^2 \left| Y^{(2)} \right|^2 + J^2 B^2 \left| Z^{(2)} \right|^2 \right]
\end{aligned}
\tag{109}
$$

$$
\begin{aligned}
X^{(1)} &= X^{(2)} = X^{(3)} \\
Y^{(1)} &= Y^{(2)} \\
Z^{(1)} &= Z^{(2)} .
\end{aligned}
\tag{110}
$$

The regularity condition on the axis can be written

$$X^{(3)}(\psi = 0) = 0 . \tag{111}$$

In a wall constrained case the vacuum energy is omitted and there is the additional boundary condition at the plasma surface:

$$X^{(3)}(\psi = \psi_s) = 0 . \tag{112}$$

The periodicity conditions in χ are

$$\begin{aligned} X^{(1)}(\psi, \chi = 0) &= X^{(1)}(\psi, \chi = 2\pi) \\ Y^{(1)}(\psi, \chi = 0) &= Y^{(1)}(\psi, \chi = 2\pi) \\ Z^{(1)}(\psi, \chi = 0) &= Z^{(1)}(\psi, \chi = 2\pi) . \end{aligned} \tag{113}$$

All that has been done is to rewrite the exact Lagrangian in a more complicated manner. Note that the quantities with the upper index (1) appear with a χ- derivative, the upper index (2) with the function and the index (3) with a ψ- derivative.

We will now consider the numerical approximation. For that purpose we define in Fig. 17 the location of the nodal values for the functions. The idea is to first make a finite element expansion of the variables $X^{(1)}$, $X^{(2)}$, $X^{(3)}$, $Y^{(1)}$, $Y^{(2)}$, $Z^{(1)}$ and $Z^{(2)}$ without enforcing the identities (110) between these function. Calling $e_{i+\frac{1}{2}j}$ the basis functions for $X^{(1)}$, $Y^{(1)}$ and $Z^{(1)}$, $f_{i+\frac{1}{2}\ j+\frac{1}{2}}$ the basis functions for $X^{(2)}$, $Y^{(2)}$ and $Z^{(2)}$ and $g_{ij+\frac{1}{2}}$ the basis functions for $X^{(3)}$ the variables are then expanded as:

$$X^{(1)} = \sum_{i=0}^{N_\psi - 1} \sum_{j=0}^{N_\chi} X_{i+\frac{1}{2}\, j}\; e_{i+\frac{1}{2}\, j}$$

$$X^{(2)} = \sum_{i=0}^{N_\psi - 1} \sum_{j=0}^{N_\chi - 1} X_{i+\frac{1}{2}\, j+\frac{1}{2}}\; \phi_{i+\frac{1}{2}\, j+\frac{1}{2}}$$

$$X^{(3)} = \sum_{i=0}^{N_\psi} \sum_{j=0}^{N_\chi - 1} X_{i\, j+\frac{1}{2}}\; g_{i\, j+\frac{1}{2}}$$

$$Y^{(1)} = \sum_{i=0}^{N_\psi - 1} \sum_{j=0}^{N_\chi} Y_{i+\frac{1}{2}\, j}\; e_{i+\frac{1}{2}\, j} \qquad (114)$$

$$Y^{(2)} = \sum_{i=0}^{N_\psi - 1} \sum_{j=0}^{N_\chi - 1} Y_{i+\frac{1}{2}\, j+\frac{1}{2}}\; \phi_{i+\frac{1}{2}\, j+\frac{1}{2}}$$

$$Z^{(1)} = \sum_{i=0}^{N_\psi - 1} \sum_{j=0}^{N_\chi} Z_{i+\frac{1}{2}\, j}\; e_{i+\frac{1}{2}\, j}$$

$$Z^{(2)} = \sum_{i=0}^{N_\psi - 1} \sum_{j=0}^{N_\chi - 1} Z_{i+\frac{1}{2}\, j+\frac{1}{2}}\; \phi_{i+\frac{1}{2}\, j+\frac{1}{2}} \; .$$

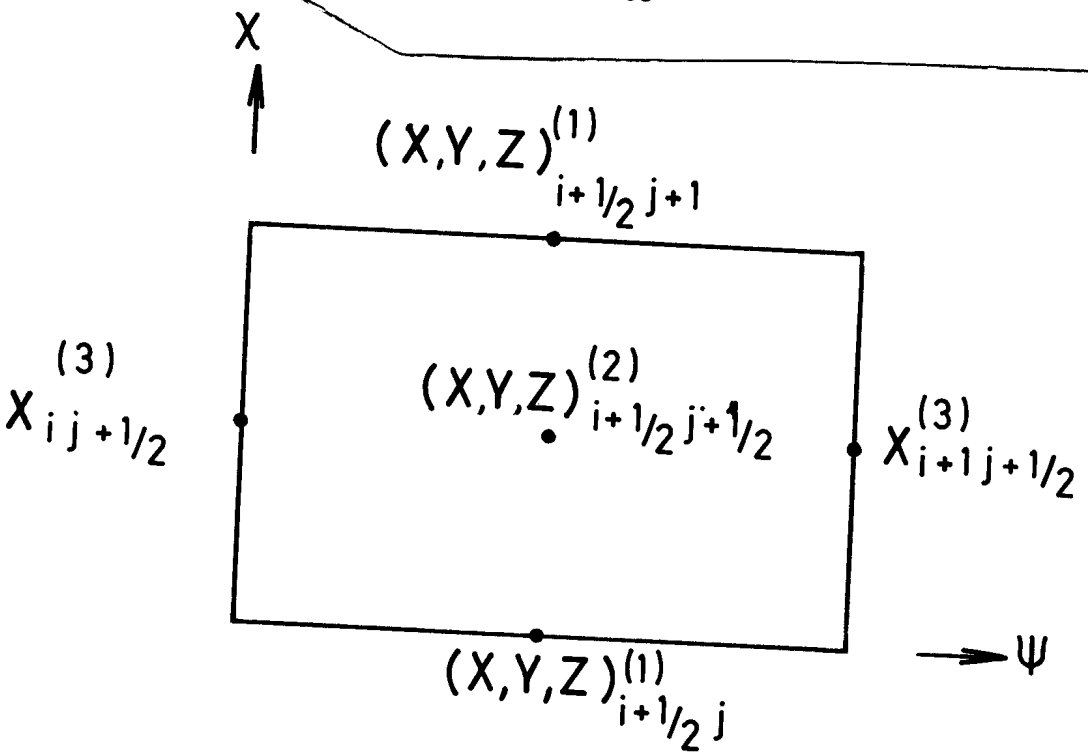

Figure 17: Position of the nodal values in a mesh cell for the "finite element description" of the finite hybrid elements.

As a lowest order approximation, we choose for $e_{i+\frac{1}{2}j}(\chi)$ a function linear in χ and piecewise constant in ψ (see e_y in Fig. 11). The χ derivative of such an element is piecewise constant. A similar roof function, linear in ψ and constant in χ, is used for $g_{ij+\frac{1}{2}}(\psi)$, such that the ψ derivative be piecewise constant. The basis for $f_{i+\frac{1}{2}\ j+\frac{1}{2}}$ is piecewise constant, extending only over a cell. With this choice of variables and basis functions each term in

$$\underline{\nabla}\cdot\underline{\xi} = \frac{\partial \chi^{(3)}}{\partial \psi} + in\, Y^{(2)} + \frac{\partial z^{(1)}}{\partial \chi} \qquad (115)$$

is represented by a piecewise function, thus satisfying the fundamental requirement that $\underline{\nabla}\cdot\underline{\xi}$ can vanish everywhere.

The regularity and boundary conditions, eqs. (43, 44) become

$$X^{(3)}_{0\,j+1/2} = 0 \qquad 0 \le j \le N_x - 1$$
$$X^{(3)}_{N_\psi\, j+1/2} = 0 , \tag{116}$$

and the periodicity conditions in χ yield

$$X^{(1)}_{i+1/2\;0} = X^{(1)}_{i+1/2\;N_x}$$
$$Y^{(1)}_{i+1/2\;0} = Y^{(1)}_{i+1/2\;N_x} \qquad 0 \le i \le N_\psi - 1 \tag{117}$$
$$Z^{(1)}_{i+1/2\;0} = Z^{(1)}_{i+1/2\;N_x} .$$

Since the functions have different functional dependence it is not possible to satisfy the identities (110) everywhere. The idea is to impose these relations only at a certain number of points, depending on the order of the approach. In our case we identify the functions at one point per mesh cell (at the mid points). This gives the required additional relations:

$$X^{(2)}_{i+1/2\;j+1/2} = \frac{X^{(3)}_{i\,j+1/2} + X^{(3)}_{i+1\;j+1/2}}{2}$$
$$\frac{X^{(1)}_{i+1/2\,j} + X^{(1)}_{i+1/2\,j+1}}{2} = X^{(2)}_{i+1/2\;j+1/2} \tag{118}$$

$$Y^{(2)}_{i+\frac{1}{2}\,j+\frac{1}{2}} = \frac{Y^{(1)}_{i+\frac{1}{2}\,j} + Y^{(1)}_{i+\frac{1}{2}\,j+1}}{2}$$

$$Z^{(2)}_{i+\frac{1}{2}j+\frac{1}{2}} = \frac{Z^{(1)}_{i+\frac{1}{2}j} + Z^{(1)}_{i+\frac{1}{2}j+1}}{2} \quad . \tag{118}$$

Note that the independent variables are now $X^{(3)}_{ij+\frac{1}{2}}$, $Y^{(1)}_{i+\frac{1}{2}j}$ and $Z^{(1)}_{i+\frac{1}{2}j}$.

The variational form given by eq. (109) contains $7 \cdot N_\psi \cdot N_\chi + 3 \cdot N_\psi + N_\chi$ variables when the displacement vector and its derivatives are expanded as prescribed by eqs. (114). The regularity condition (43) fixes N_χ variables. For a wall constrained plasma the boundary condition (44) fixes also N_χ variables. The periodicity conditions, eqs. (117) eliminate $3 \cdot N_\psi$ unknowns and the identities (118) reduce the number of unknowns by $4 \cdot N_\psi \cdot N_\chi$. For the case with a vacuum region there remain $3 \cdot N_\psi \cdot N_\chi$ independent nodal values and for a wall constrained case there are $3 \cdot N_\psi \cdot N_\chi - N_\chi$ independent nodal values.

This finite element description of the finite hybrid elements is identical to the finite differences description, provided that $X^{(3)}_{ij+\frac{1}{2}}$ in the finite element description is replaced by $(X_{ij} + X_{ij+1})/2$ in the finite differences description.

3. Application to the Cylindrical Case and Comparison with Regular Elements

We apply this two-dimensional finite hybrid element method to the wall constrained cylindrical test case. Both m = 1 and m = 2 are considered. In the m = 1 case the parameters are the same as in chapter V, namely $j_z = 0.4\ T/r_s$ and $N_\psi = 12$. Figure 18 a-c shows the results for this m = 1 case. The square of the growth rates Γ^2 of the internal modes is plotted versus $q \equiv krB_z/B_\theta = 5\ kr_s$. The solid curves represent the results obtained

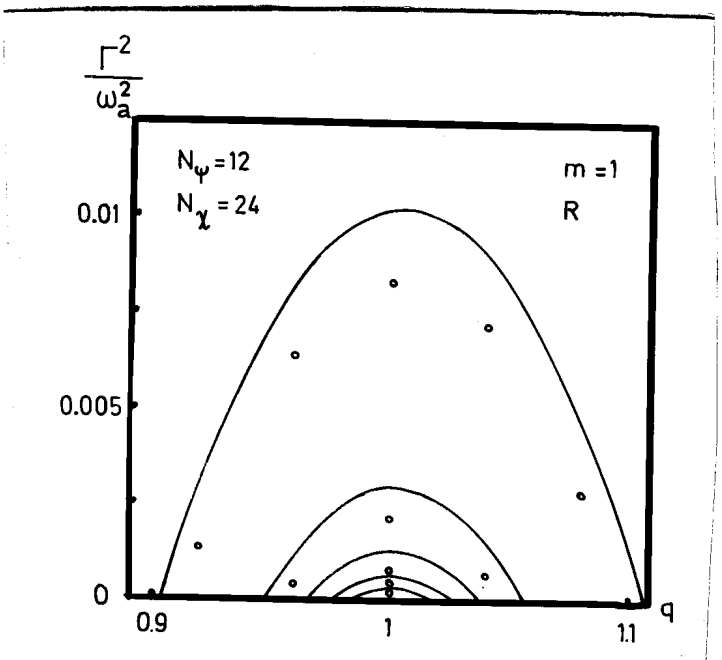

Fig. 18: Comparison of the first 5 fundamental modes of the wall constrained cylindrical test case using

(a) regular finite elements

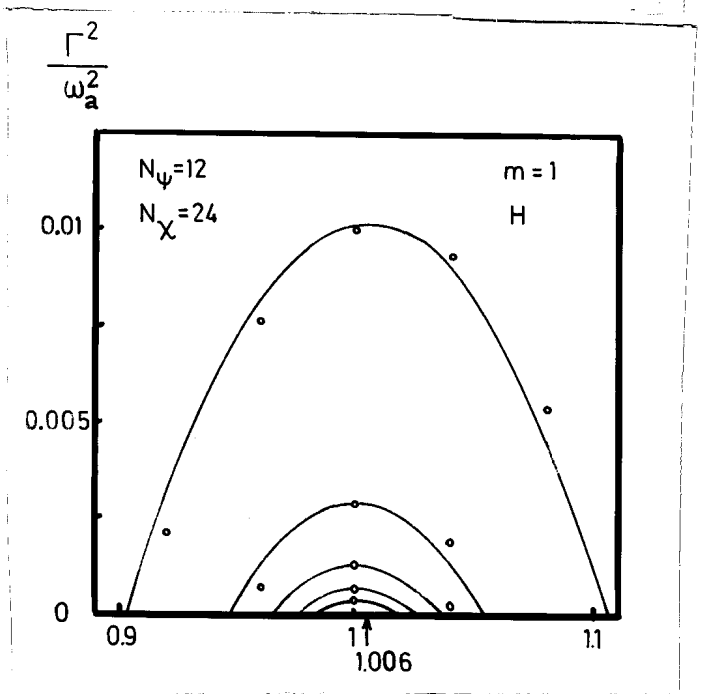

(b) finite hybrid elements

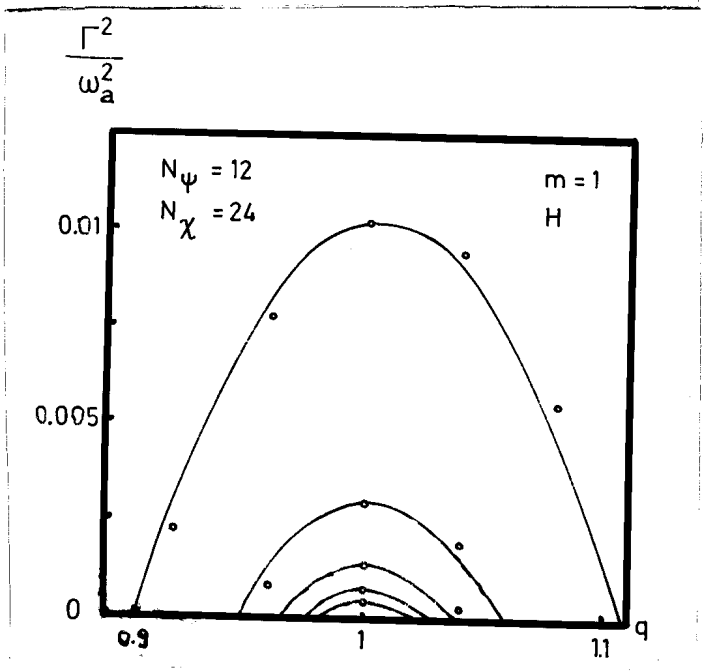

(c) finite hybrid elements with a piecewise constant equilibrium.

with three different 2-D methods:

(a) Regular finite elements as defined in eq. (90).

(b) Finite hybrid elements as described in eqs. (114).

(c) Finite hybrid elements with equilibrium quantities taken constant in each mesh cell.

Making use of the symmetry, only $N_\psi = 12$ intervals are used in half the range $0 \leq \chi \leq \pi$. There is little difference between the last two methods although the modes in Fig. 18c are slightly more unstable than those in Fig. 18b. The results in Fig. 18a show a rather large discrepancy.

In all three cases the spectra are not polluted. This can be seen when studying the unstable part of the spectra at $q = 1$. Here an infinite number of unstable fundamental modes should be observed. Numerically, this means that $N_\psi - 1$ modes are unstable when N_ψ radial intervals are taken. Thus, at $q = 1$ with $N_\psi = 12$ one should find 11 unstable Alfvèn modes. It is surprising that one obtains 9 of them in the highly stabilized case (a). The stabilizing effect due to the coupling between the modes must therefore diminish for higher fundamental Alfvèn modes. From these results we expect that the coupling effect, observed in Fig. 18a, disappears when an infinite number of mesh cells are taken. In the cases (b) and (c) only 8 unstable displacement vectors are found at $q = 1$. This comes from the fact that there is a shift of the growth rate curves by 0.6 % towards higher q-values. When one counts the number of negative values of ω^2 at $q = 1.006$, one finds all the 11 modes unstable. This shift of the whole spectrum depends on the value of azimuthal interval number N_χ.

The agreement of the results obtained by the last two methods has important practical implications. In case (c) the equilibrium quantities have to be known only in the center of the mesh cells. This is an advantage which becomes crucial when one studies numerically determined equilibria.

It is more difficult to calculate the unstable part of the m = 2 spectrum. The maximum growth rate is 8 times smaller than that obtained in the m = 1 spectrum, and the eigenfunction varies twice as rapidly in the angular direction. No unstable modes are found in this case with the regular finite elements method, even when 20 azimuthal intervals are taken in half the range. Using finite hybrid elements, however, we obtain, with high accuracy, the whole unstable part of the spectrum as shown in Fig. 19. The shift towards higher 9 values is more pronounced for a fixed number of mesh points. At q = 2.017, for example, we again find that all 11 fundamental modes are unstable ! The cross at the upper right hand corner of Fig. 19 at q = 2.11

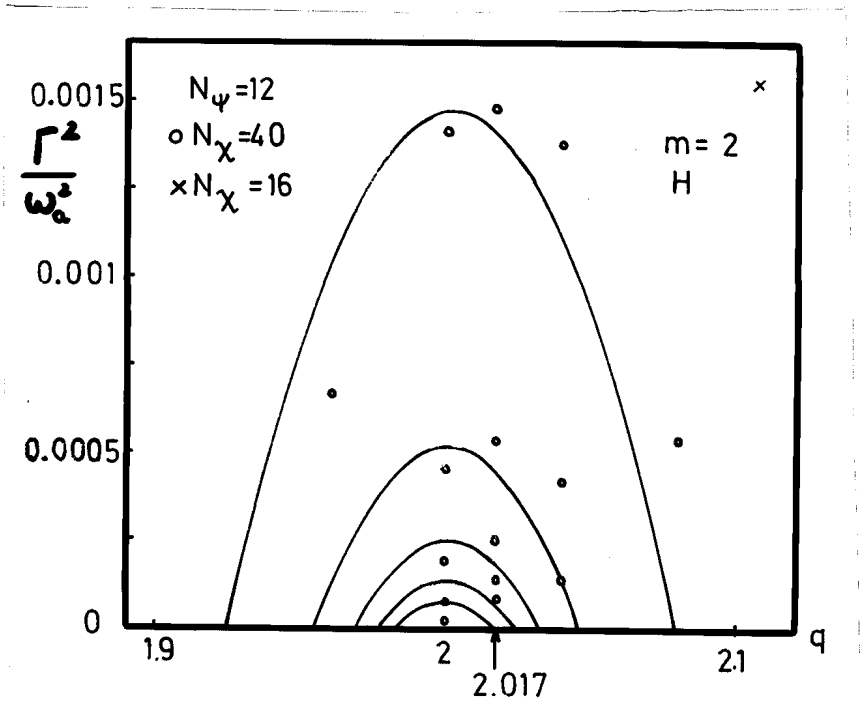

Figure 19: Unstable part of the m = 2 spectrum of the wall constrained cylindrical test case, kr_s= 0.2. The solid curves represent the "exact" 1-D results. The small circles are the results of the 2-D calculations performed with the finite hybrid element method using a piecewise constant equilibrium, N_χ = 20. The cross at the upper right and corner at q = 2.11 is the maximum of the most unstable mode obtained with N_χ = 8. No unstable modes are obtained with regular finite elements.

is the maximum value of Γ^2 obtained when taking only $N_\chi = 8$ azimuthal intervals. This value differs only by 5 % from the maximum obtained with the 1-D code. Note that the maximum growth rate is overestimated. This can naturally never happen with regular finite elements.

Let us now study the dependence of the shifting as a function of the number of azimuthal intervals. The relative shift in q as a function of $1/N_\chi^2$ is shown in Fig. 20 for m = 2. The straight line corresponds to a quadratic convergence of the shifted discretized spectrum. The convergence is to the "exact" 1-D result.

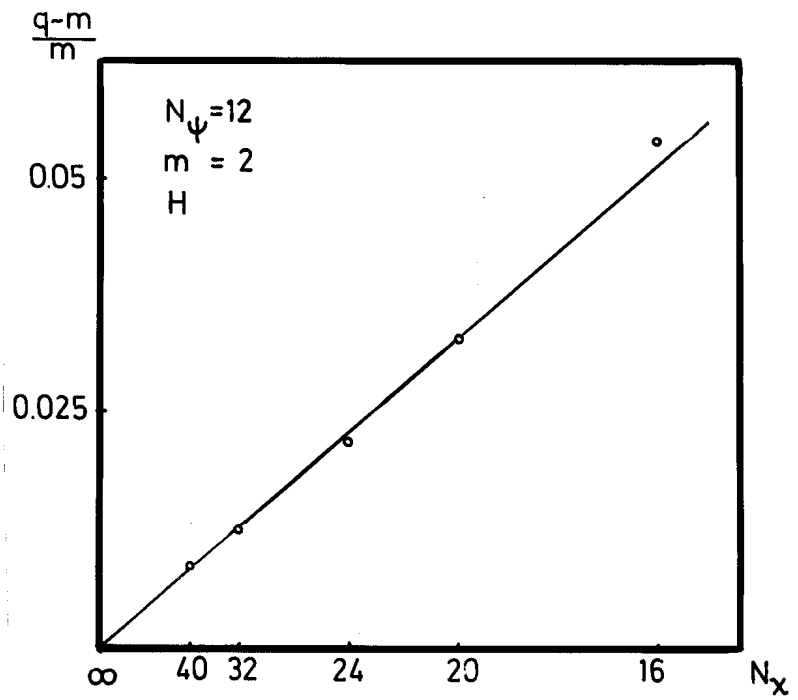

Figure 20: The relative shift (q-m)/m of the spectrum calculated with finite hybrid elements and a piecewise constant equilibrium is plotted versus $1/N_\chi^2$. The straight line corresponds to a quadratic convergence.

These results show that the finite hybrid element method can indeed reproduce the weakly growing internal modes with only a few mesh cells. The shift in q of the spectrum is not important as long as the characteristic features of the spectrum are well reproduced, namely the growth rates and the eigenfunctions.

From the technical point of view this method has advantages compared to the regular finite elements, such as:

- The sizes of the matrices are smaller for the same number of mesh cells.
- No integration has to be performed if the equilibrium is taken piecewise constant.
- The method is particularly well suited for the stability calculation of numerically determined equilibria.

4. Prospects for the Future

The last version of the 2-D code which uses finite hybrid elements has been tried on a simple test case. We feel confident that it will work equally well in toroidal geometry. Unfortunately no toroidal equilibrium is known for which it is possible to calculate analytically the spectrum. A workshop on stability codes was arranged during the last European Conference on Plasma Physics and Controlled Fusion [30] during which a standard toroidal test case was defined. This test case will serve to compare the results of all the stability codes being presently developped in the world.

Concerning our approach the code will still evolve. The numerical computation of the Green function for the vacuum contribution in the general toroidal case has to be added. A switch to a non-orthogonal mesh, using the so-called "natural coordinate system" proposed by the Princeton group [28], will be tried in order to avoid the singularity at the magnetic

axis due to the behaviour of the Jacobian J. Also it will be interesting to use higher order basis functions in the finite hybrid elements method. The polynomials for the functions and their derivatives will be chosen in such a way that each of the quadratic terms in eqs. (26, 39-42) is expressed by a polynomial of the same order in Ψ and χ . The connection of the functions with their derivatives have then to be done in a sufficient number of points per mesh cell.

VII. CONCLUSION

The development of a general purpose numerical code, capable to compute the unstable part of the MHD spectrum of any axisymmetric toroidal configuration, has revealed itself to be a much harder problem than anticipated. In low-β configurations even the largest growth rates are small compared with the characteristic frequency of the system. The internal modes have even smaller growth rates. The presence of the continua extending to $\omega^2 = 0$ is another source of numerical problems. In order to be able to obtain useful results these difficulties have been identified and solved one by one, by developping unconventional numerical methods.

The first difficulties appear already in the one-dimensional cylindrical case. A so-called "spectrum pollution" [22] was observed when linear finite elements were used for all vector components in a Ritz-Galerkin expansion. A strong mixing between the Alfvèn and the fast modes [8, 29] was the cause of this pollution. As a result it was impossible to obtain the unstable part of the spectrum in the low-β limit. This difficulty was removed by a suitable choice of different basis functions for different vector components [9].

The same idea of choosing different basis functions for different components of the displacement vector was then tried in two dimensions. This is the so-called regular finite element approach. No pollution has been observed in the test case considered [21] and the kink modes were well reproduced. But the weakly growing internal modes were still not well represented. This was traced to a bad representation of the operator $\underline{B} \cdot \underline{\nabla}$.

A new numerical scheme, which we propose to call "finite hybrid elements", has been tried. In a test calculation this method has reproduced the weakly growing modes with high accuracy already with a few points. We believe that this method will ultimately give the most efficient toroidal stability code.

ACKNOWLEDGEMENTS

The author is greatfully indebted to D. Berger and Drs. J. Rappaz and F. Troyon for their fruitful collaboration throughout the whole work. Dr. K. Appert joined our group for the 1-D calculations and contributed to the 2-D work with helpful suggestions and critical comments. We would also like to thank Prof. Dr. J. Descloux, Dr. J.M. Greene, Dr. F. Hofmann, Prof. Dr. K.W. Morton, A. Pochelon, Dr. K.V. Roberts, Dr. J.S. Soulé, Dr. J. Vaclavik and Prof. E.S. Weibel for very stimulating discussions.

Improving the english of this work is due to Dr. A. Kritz. Miss Nicole Marendaz has carefully typewritten the text and K. Hruska drawn the figures.

We would also like to mention the programming support by D. Borel, F. Debonneville and R. Schreiber. Finally we are indebted to the staff of the computing center who gave us judicious advice on many occasions and handled our jobs.

REFERENCES

[1] B.B. Kadomtsev, in "Reviews of Plasma Physics", edited by M.A. Leontovich (Consultants Bureau, N.Y. 1966), Vol. 2, 155

[2] B.R. Suydam, in Proc. of the 2nd International Conf.on the Peaceful Uses of Atomic Energy 31 (1958), 157

[3] C. Mercier, Nucl.Fusion 1 (1960), 47

[4] C. Mercier, Soubbaramayer, 7th Europ.Conf.on Contr.Fusion and Plasma Phys. Vol. I (1975), 8

[5] A. Sykes, J. Wesson, private communication

[6] R.C. Grimm, J.M. Greene, J.L. Johnson, private communication

[7] K. Hain, R. Lüst, Z.Naturforschung 13a, (1958), 936

[8] T. Takeda, Y. Shimomura, M. Ohta, M. Yoshikawa, Phys.Fluids 15 (1972). 2193

[9] K. Appert, D. Berger, R. Gruber, J.Comp.Phys. 18 (1975), 284

[10] G. Laval, R. Pellat, J.S. Soulé, Phys.Fluids 17 (1974), 835

[11] M.N. Bussac, D. Edery, G. Laval, R. Pellat, J.L. Soulé, 7th Europ.Conf.on Contr.Fusion and Plasma Phys. Vol. I (1975), 100

[12] G. Laval, Phys.Rev.Letters 34 (1974), 1316

[13] A. Sykes, J. Wesson, Nucl.Fusion 14 (1974), 645

[14] G. Bateman, W. Schneider, W. Grossmann, Nucl.Fusion 14 (1974), 669

[15] D.A. Baker et al., 7th Europ.Conf.on Contr.Fusion and Plasma Phys. Vol. I (1975), 41

[16] R.D. Richtmeyer, K.W. Morton, "Difference Methods for Initial-Value Problems", 2nd edition, Interscience Publishers, N.Y. 1967

[17] J. Wooten, H.R. Hicks, G. Bateman, R.A. Dory, ORNL TM 4784 (1974)

[18] A. Sykes, J.A. Wesson, 7th Europ.Conf.on Contr.Fusion and Plasma Phys. Vol. I (1975), 111

[19] O.C. Zienkiewicz, "The Finite Element Method in Structural and Continuum Mechanics", McGraw-Hill, N.Y. 1971

[20] K. Appert, D. Berger, R. Gruber, F. Troyon, K.V. Roberts, Computer Phys.Commun. 10 (1975), 11

[21] R. Gruber, K. Appert, D. Berger, F. Debonneville, F. Troyon, 7th Europ.Conf.on Contr.Fusion and Plasma Phys. Vol. I (1975), 108

[22] J. Rappaz, Thesis, to appear and Journées Eléments Finis à Rennes (1975)

[23] M. Bineau, Nucl.Fusion 2 (1962), 130

[24] I.B. Bernstein, E.A. Frieman, M.D. Kruskal, R.M. Kulsrud, Proc.Roy. Soc. (London), Ser. A244 (1958), 39

[25] W.A. Newcomb, Ann.Phys. (N.Y.) 10 (1960), 232

[26] R.L. Dewar, R.C. Grimm, J.L. Johnson, E.A. Frieman, J.M. Greene, P.H. Rutherford, Phys.Fluids 17 (1974), 930

[27] R.L. Dewar, J.M. Greene, R.C. Grimm, J.L. Johnson, J.Comp.Phys. 17 (1975)

[28] R.C. Grimm, J.M. Greene, J.L. Johnson, in "Method of Computational Physics" edited by B. Alder, S. Fernbach and M. Rotenberg (Academic Press, N.Y.), Vol. 16, chapter 4

[29] K. Appert, D. Berger, R. Gruber, F. Troyon, J. Rappaz, ZAMP 25 (1974), 229

[30] Workshop on MHD stability at the 7th Europ.Conf.on Contr.Fusion and Plasma Phys. Lausanne (1975)

[31] E.S. Weibel, Am.Jnal.of Phys. Vol. 36, No 12 (1968)

[32] G. Schmidt, "Physics of High Temperature Plasmas", Academic Press, N.Y. 1966

[33] C. Mercier "Lectures in Plasma Physics" EUR 5127e (1974) Commission of the European Communities

[34] K. Appert, R. Gruber, J. Vaclavik, Phys.Fluids 17 (1974), 1471

[35] J.P. Goedbloed, H.J.L. Hagebeuk, Phys.Fluids 15 (1972), 1090

[36] J.P. Goedbloed, Phys.Fluids 18 (1975), 1258

[37] W.I. Smirnov, Lehrgang der höheren Math. V, (Berlin, 1962) Deutscher Verlag der Wissenschaften

[38] V.D. Shafranov, Sov.Phys.Tech.Phys. 15 (1970), 175

[39] K. Yosida, Functional Analysis (Berlin, 1968) Springer-Verlag

[40] E. Stiefel, Einführung in die num.Math. (Stuttgart, 1961), B.G. Teubner Verlagsgesellschaft

[41] J.H. Wilkinson, The Algebraic Eigenvalue Problem (Oxford, 1965) Clarendon Press

[42] R. Gruber, Computer Phys.Commun. 10 (1975), 30

[43] A. Pochelon, R. Keller, F. Troyon, R. Gruber, 7th Europ.Conf.on Contr.Fusion and Plasma Phys. Vol. I (1975), 157

[44] D. Borel, K. Appert, D. Gruber, F. Troyon, ZAMP 26 (1975), 656

[45] K. Appert, D. Berger, R. Gruber, Physics Letters, 46A (1974), 339

[46] K. Appert, R. Gruber, F. Hofmann, to be published

[47] I.R. Jones, to be published

[48] R. Gajewski, Phys.Fluids 15 (1972), 70

[49] E. Stiefel, Mitteilungen aus dem Institut für angewandte Mathematik, Nr 8 (1959) Birkhäuser Verlag, Basel

APPENDIX

Table of Symbols

a	small axis of the plasma surface
$\mathcal{A}$	small axis of the conducting wall
$\underline{B}$	total magnetic field
B	poloidal equilibrium magnetic field
$\underline{B_o}$	equilibrium magnetic field
B_o^2	$B_\theta^2 + B_z^2$
B_r	radial magnetic field
$\underline{B_r}$	vacuum magnetic field
B_z	axial equilibrium magnetic field
B_θ	azimuthal equilibrium magnetic field
$\mathcal{B}$	big axis of the conducting wall
β	gas pressure at axis over magnetic pressure at surface
$C_2(\Omega)$	space for Y and Z
$C_{i+\frac{1}{2}}$	constant 1-D basis function
Γ	growth rate
γ	ratio of specific heat
$\gamma_{m,\alpha}$	α^{th} zero of J_m'
D	$\underline{\nabla} \cdot \underline{\xi}$
$\underline{d\ell}$	line element
$d\sigma_s$	surface element
$d\tau$	volume element
δ	perturbation
∂	partial derivative
$\underline{E}$	total electric field
$\underline{E_o}$	equilibrium electric field
e_j	linear 1-D basis function
e_ℓ^x	basis function for X attributed to mesh point ℓ

e_x^{ij}	basis function for X at (ψ_i, χ_j)
$\underline{\hat{e}}_\chi$	poloidal unity vector
$\underline{\hat{e}}_\psi$	radial unity vector
$\underline{\hat{e}}_\theta$	toroidal unity vector
ϵ	ellipticity
$\underline{F}$	plasma force operator
F	$k B_z + \frac{m}{r} B_\theta$
f^{ij}	basis function for Y and Z at (ψ_i, χ_j)
f_ℓ^y	basis function for Y attributed to mesh point ℓ
f_ℓ^z	basis function for Z attributed to mesh point ℓ
ϕ	scalar potential
$G(\underline{r}/\underline{r_s})$	Green function
H	space such that $\hat{\underline{\xi}} \in H$
H^1	Sobolev space
η	transformed 1-D vector component
i	ψ mesh counter
$\underline{J}$	total current density
J	Jacobian
$\underline{J_o}$	equilibrium current density
J_m'	radial derivative of Bessel m
J_z	normalized axial equilibrium current density
j	axial equilibrium current density
j	χ mesh counter
j_z	axial equilibrium current density
k	axial wave number
χ	poloidal coordinate
L	Lagrangian
L_2	space of square integrable functions
ℓ	general mesh point counter

m	poloidal wave number
N_χ	number of χ intervals
N_ψ	number of ψ intervals
n	toroidal wave number
$\underline{\hat{n}}$	unity vector normal to the flux surfaces
P	total perturbed pressure
p	total pressure
p_o	equilibrium pressure
ψ	surface of constant magnetic flux
ψ_s	ψ at plasma surface
q	safety factor
R	position of the magnetic axis
$\underline{r}$	perturbed location
r	distance from the symmetricity axe
$\underline{r_o}$	unperturbed location
r_j	location of interval point j
$\underline{r_s}$	location of the plasma surface
r_w	position of the conducting wall
ρ	total mass density
ρ_o	equilibrium mass density
T	toroidal equilibrium magnetic field
t	time
θ	toroidal or polar angle
U	transformation matrix
V	discretized subspace ($V \subset H$)
V_1	discretized subspace for ξ_1 or X
V_2	discretized subspace for ξ_2 or Y
V_3	discretized subspace for ξ_3 or Z

$\underline{v}$	velocity
W_k	perturbed kinetic energy
W_p	perturbed potential energy
W_v	perturbed vacuum energy
Ω	plasma region
ω	eigenfrequency
$\omega_3 \ldots \omega_7$	separators
ω_A	frequency of Alfvèn continuum
ω_S	frequency of slow wave continuum
X	transformed radial complex displacement
$X^{(1)}$	X component for χ derivative
$X^{(2)}$	X component for function value
$X^{(3)}$	X component for ψ derivative
X_ℓ	value of X at mesh point ℓ
X_{ij}	X component at (ψ_i, χ_j)
$\underline{\xi}$	displacement vector
$\hat{\underline{\xi}}$	transformed $\underline{\xi}$
ξ_1	transformed ξ_r
ξ_2	transformed ξ_θ
ξ_3	transformed ξ_z
ξ_n	displacement component // to $\underline{\hat{n}}$
$\hat{\underline{\xi}}^n$	transformed total displacement
ξ_r	radial displacement component
ξ_z	longitudinal displacement component
ξ_θ	azimuthal or toroidal displacement component
ξ_χ	poloidal displacement component
ξ_ψ	radial displacement component

Y	transformed complex toroidal displacement
$Y^{(1)}$	Y component for χ derivative
$Y^{(2)}$	Y component for function value
Y_{ℓ}	value of X at mesh point ℓ
Y_{ij}	Y component at (ψ_i, χ_j)
Z	transformed complex toroidal displacement
$Z(r)$	solution of Bessel's equation of order 0
$Z^{(1)}$	Z component for χ derivative
$Z^{(2)}$	Z component for function value
Z_{ℓ}	value of Z at mesh point ℓ
Z_{ij}	Z component at (ψ_i, χ_j)
z	location in axial direction
ζ	transformed 1-D vector component